

THE NEXT GENERATION FORNAX SURVEY (NGFS): II. THE CENTRAL DWARF GALAXY POPULATION

PAUL EIGENTHALER^{1,14}, THOMAS H. PUZIA¹, MATTHEW A. TAYLOR², YASNA ORDENES-BRICEÑO^{1,6}, ROBERTO P. MUÑOZ¹, KAREN X. RIBBECK¹, KARLA ALAMO-MARTÍNEZ¹, HONGXIN ZHANG¹, SIMÓN ÁNGEL¹, MASSIMO CAPACCIOLI⁴, PATRICK CÔTÉ⁵, LAURA FERRARESE⁵, GASPAR GALAZ¹, EVA K. GREBEL⁶, MAREN HEMPEL¹, MICHAEL HILKER⁷, ARIANE LANÇON⁸, STEFFEN MIESKE³, BRYAN MILLER⁹, MAURIZIO PAOLILLO¹⁰, MATHIEU POWALKA⁸, TOM RICHTLER¹¹, JOEL ROEDIGER⁵, YU RONG^{1,14,15}, RUBEN SÁNCHEZ-JANSSEN¹², CHELSEA SPENGLER¹³

¹Instituto de Astrofísica, Pontificia Universidad Católica de Chile, Av. Vicuña Mackenna 4860, 7820436 Macul, Santiago, Chile

²Gemini Observatory, Northern Operations Center, 670 North A'ohoku Place, Hilo, HI 96720, USA

³European Southern Observatory, 3107 Alonso de Córdova, Vitacura, Santiago

⁴INAF-Osservatorio Astronomico di Capodimonte, Salita Moiariello 16, 80131, Naples, Italy

⁵NRC Herzberg Astronomy and Astrophysics, 5071 West Saanich Road, Victoria, BC V9E 2E7, Canada

⁶Astronomisches Rechen-Institut, Zentrum für Astronomie der Universität Heidelberg, Mönchhofstr. 12-14, D-69120 Heidelberg, Germany

⁷European Southern Observatory, Karl-Schwarzschild-Str. 2, D-85748 Garching, Germany

⁸Observatoire astronomique de Strasbourg, Université de Strasbourg, CNRS, UMR 7550, 11 rue de l'Université, F-67000 Strasbourg, France

⁹Gemini Observatory, South Operations Center, Casilla 603, La Serena, Chile

¹⁰Department of Physics, University of Naples Federico II, C.U. Monte Sant'Angelo, via Cinthia, 80126, Naples, Italy

¹¹Departamento de Astronomía, Universidad de Concepción, Casilla 160-C, Concepción, Chile

¹²STFC UK Astronomy Technology Centre, Royal Observatory, Blackford Hill, Edinburgh, EH9 3HJ, UK

¹³Department of Physics and Astronomy, University of Victoria, Victoria, BC V8P 5C2, Canada

¹⁴Chinese Academy of Sciences South America Center for Astronomy and China-Chile Joint Center for Astronomy, Camino El Observatorio 1515, Las Condes, Santiago, Chile

¹⁵National Astronomical Observatories, Chinese Academy of Sciences, 20A Datun Road, Chaoyang District, Beijing 100012, China

To be submitted to The Astrophysical Journal

ABSTRACT

We present a photometric study of the dwarf galaxy population in the core region ($\lesssim r_{\text{vir}}/4$) of the Fornax galaxy cluster based on deep $u'g'i'$ photometry from the *Next Generation Fornax Cluster Survey*. All imaging data were obtained with the Dark Energy Camera mounted on the 4-meter Blanco telescope at the Cerro-Tololo Interamerican Observatory. We identify 258 dwarf galaxy candidates with luminosities $-17 \lesssim M_{g'} \lesssim -8$ mag, corresponding to typical stellar masses of $9.5 \gtrsim \log \mathcal{M}_*/M_\odot \gtrsim 5.5$, reaching ~ 3 mag deeper in point-source luminosity and ~ 4 mag deeper in surface-brightness sensitivity compared to the classic Fornax Cluster Catalog. Morphological Sérsic analysis shows that the dwarf galaxy surface-brightness profiles are well represented by single-component Sérsic models with average Sérsic indices of $\langle n \rangle_{u',g',i'} = (0.78 - 0.83) \pm 0.02$, and average effective radii of $\langle r_e \rangle_{u',g',i'} = (0.67 - 0.70) \pm 0.02$ kpc. Color-magnitude relations indicate a flattening of the galaxy red sequence at faint galaxy luminosities, similar to the one recently discovered in the Virgo cluster. A comparison with population synthesis models and the galaxy mass-metallicity relation reveals that the average faint dwarf galaxy is likely older than ~ 5 Gyr. We study galaxy scaling relations between stellar mass, effective radius, and stellar mass surface density over a stellar mass range covering six orders of magnitude. We find that over the sampled stellar mass range several distinct mechanisms of galaxy mass assembly can be identified: *i*) dwarf galaxies assemble mass inside the half-mass radius up to $\log \mathcal{M}_* \approx 8.0$, *ii*) isometric mass assembly in the range $8.0 \lesssim \log \mathcal{M}_*/M_\odot \lesssim 10.5$, and *iii*) massive galaxies assemble stellar mass predominantly in their halos at $\log \mathcal{M}_* \approx 10.5$ and above.

Subject headings: galaxies: clusters: individual (Fornax) — galaxies: dwarf — galaxies: elliptical and lenticular, cD — galaxies: fundamental parameters — galaxies: stellar content

1. INTRODUCTION

Representing the current standard theory of structure formation in the universe, the Lambda Cold Dark Matter (Λ CDM) model is the simplest one that is in general agreement with observations, e.g. the large-scale structure distribution of galaxies and their scaling relations. Although the Λ CDM paradigm is consistent with many of these phenomena at large scales, tensions with observations arise at mass scales of $\lesssim 10^9 M_\odot$, where Λ CDM predicts many more DM dominated dwarf galaxy haloes than are actually observed around giant galaxies. This discrepancy between the numbers of predicted and observed dwarfs is generally referred to as the *missing satellites problem* (Moore et al. 1999; Klypin

et al. 1999) and its origin is still unclear. Either the predictions of Λ CDM are not reliable – possibly arising from the spatial resolution limits and the treatment of baryonic physics processes – or many faint dwarf galaxies have simply not yet been discovered. It was already pointed out early on that various baryonic effects like the impact of reionization indeed play a significant role (Bullock et al. 2001). Modern Λ CDM simulations that do account for a variety of baryonic effects including local and global reionization, star formation and feedback, tidal effects (e.g. Guo et al. 2011; Brooks et al. 2013; Sawala et al. 2015, 2016) typically achieve rather good agreement with the observed (dwarf) galaxy luminosity function. Another interpretation is that the large majority of low-mass DM haloes have been very inefficient at star formation.

It is now well-established that dwarf galaxies are predomi-

nantly found in galaxy group and cluster environments which, respectively, tend to host dwarfs of differing morphological types. For example, while dwarf ellipticals (dEs) dominate the cluster galaxy population, star-forming dwarf irregulars (dIrrs) are most commonly found in the field or the cluster outskirts (Sandage & Binggeli 1984; Binggeli et al. 1985, 1988), suggestive of a link between dwarf galaxy evolution and the environment they reside in (e.g. Zhang et al. 2012; Mistani et al. 2016; van de Voort et al. 2017; Read et al. 2017). This morphology-density or morphology-distance relation for dwarf galaxies appears to be largely driven by tidal and ram pressure effects (Grebel, Gallagher, & Harbeck 2003).

Dwarf galaxies have been detected throughout the Local Volume and beyond, see e.g. Binggeli & Cameron (1991); Côté et al. (1997); Karachentseva & Karachentsev (1998); Karachentseva et al. (1999); Karachentsev et al. (2000); Chiboucas et al. (2009); Müller et al. (2015) and many, many more. However, detections for the faintest dwarfs, i.e. dwarf spheroidal galaxies, have so far been mainly limited to those within the Local Group (LG) due to their low surface-brightness (e.g. McConnachie 2012). Thus, identifying and studying these faintest dwarf galaxy systems in nearby galaxy clusters and groups is crucial to constrain Λ CDM cosmology. Previous observations seem to confirm the missing satellites problem when comparing the observed galaxy numbers with the Λ CDM halo mass function in environments covering a range of galaxy densities (e.g. Pritchet & van den Bergh 1999; Trentham & Tully 2002; Ferrarese et al. 2016; Taylor et al. 2017), including rich galaxy clusters. Potentially easing some of this tension is the discovery in recent years of ultra-faint dwarf (UFD) and dwarf spheroidal (dSph) satellites throughout the Local Group (Willman et al. 2005; Belokurov et al. 2006; Zucker et al. 2006a; Belokurov et al. 2007; Zucker et al. 2007; McConnachie et al. 2009; Belokurov et al. 2010; McConnachie 2012; Belokurov et al. 2014; Bechtol et al. 2015; Drlica-Wagner et al. 2015; Koposov et al. 2015; Laevens et al. 2015; Homma et al. 2016), and rich dwarf galaxy systems around nearby giant galaxies and clusters (Karachentsev et al. 2007; Crnojević et al. 2016; Müller et al. 2015; Muñoz et al. 2015; Müller et al. 2016; Ordenes-Briceño et al. 2016; Sánchez-Janssen et al. 2016).

The newly discovered UFDs appear to be an extension of dSphs to lower luminosities (e.g. Muñoz et al. 2015), being much fainter ($M_V \gtrsim -8$ mag) and smaller ($r_{\text{eff}} \lesssim 300$ pc) than classical dSphs. UFDs have luminosities comparable to globular clusters (GCs), which are much more compact ($r_e \lesssim 10$ pc). Classical GCs typically have $M/L_V \approx 2$ (e.g. McLaughlin & van der Marel 2005; van de Ven et al. 2006; Baumgardt et al. 2009; Strader et al. 2011; Taylor et al. 2015) whereas in contrast, UFD kinematics reveal $M/L_V \gtrsim 100$, indicative of DM-dominated systems (e.g. Kleyna et al. 2005; Simon & Geha 2007). In addition to the rich populations of low-surface brightness (LSB) dwarf galaxies in the Local Volume, there have also been discoveries of *ultra-diffuse* galaxies (UDGs), first found and described by Sandage & Binggeli (1984); Impey et al. (1988); Ferguson & Sandage (1988); Bothun et al. (1991). More recent discoveries of this galaxy class have been identified in various galaxy aggregates like the Coma and Virgo galaxy clusters (van Dokkum et al. 2015; Koda et al. 2015; Mihos et al. 2015), the Pisces-Perseus supercluster (Martínez-Delgado et al. 2016), a galaxy group (Meritt et al. 2016), in the galaxy cluster Abell 2744 (Janssens et al. 2017) and Abell 168 (Román & Trujillo 2017a), and even outside of groups and clusters (Román & Trujillo 2017b). The

low stellar masses ($\sim 6 \times 10^7 M_\odot$) and large radii (1.5–4.6 kpc) of UDGs result in very low surface brightness values in the range $\mu_{0,V} \approx 26\text{--}28.5$ mag arcsec $^{-2}$, making them challenging to detect. The existence of this mysterious new galaxy class in mostly dense galaxy cluster environments prompts the obvious question of whether there might be similar populations in other galaxy aggregates, or whether they are reserved for rich galaxy clusters only.

In the present work we attempt to address these questions by investigating the properties of the low surface-brightness dwarf galaxy population in the inner region of the Fornax galaxy cluster, one of the most nearby southern galaxy clusters, using data obtained as part of the *Next Generation Fornax Survey* (NGFS). The survey constitutes of deep, wide-field, multi-passband $u'g'i'$ observations taken with the Dark Energy Camera (DECam; Flaugher et al. 2015) mounted on the 4-meter Blanco telescope at Cerro Tololo Inter-American Observatory (CTIO). Given its proximity, Fornax is a goldmine for studying the formation and evolution of galaxies and other stellar systems, such as GCs and dwarf galaxies, in a galaxy cluster environment (Muñoz et al. 2015; Iodice et al. 2016; D’Abrusco et al. 2016; Wittmann et al. 2016). Compared to its northern counterpart, the Virgo cluster, Fornax has twice the central galaxy density, half the velocity dispersion, and accordingly a distinctly lower mass ($7 \pm 2 \times 10^{13} M_\odot$; Ferguson 1989; Schubert et al. 2010). Furthermore, the core of Fornax is dynamically more evolved (Churazov et al. 2008) and its early-type (E/S0) galaxy fraction is significantly larger ($\sim 50\%$) than that of Virgo ($\sim 35\%$), considering member galaxies brighter than $M_B = -16$ mag not classified as dwarfs in the FCC (Ferguson 1989) and VCC (Binggeli et al. 1985) catalogues. Noting the above, the Fornax cluster is an excellent target to study faint baryonic sub-structures in one of the most nearby cluster environments. Throughout this work we utilize a distance modulus of 31.51 ± 0.03 mag for Fornax, corresponding to a distance of ~ 20 Mpc (Blakeslee et al. 2009). Derived magnitudes refer to the AB system.

2. OBSERVATIONS

Our imaging is conducted as part of the NGFS for which we provide an abbreviated summary here to put the present contribution into context. The NGFS is an ongoing survey of the Fornax galaxy cluster core in the optical u' , g' , and i' and the near-infrared (NIR) J and K_s filters, targeting the inner 30 deg^2 , corresponding to ~ 1 Mpc in galactocentric radius centered on the cD galaxy NGC 1399. Here we focus on the NGFS optical survey observations, which consists of nine contiguous DECam tiles, each aiming at a minimum point-source detection limit of $u' = 26.5$, $g' = 26.1$, and $i' = 25.3$ mag at $S/N = 5$ over the PSF area. With the goal of maximizing sensitivity to LSB structures in the imaging, we employ the Elixir-LSB dithering technique developed for the complementary *Next Generation Virgo Survey* (NGVS, see Ferrarese et al. 2012, for details), and use raw images processed by the DECam Community Pipeline (CP; v.2.5.0 Valdes et al. 2014) to produce fully calibrated image stacks. The CP processes the raw DECam images for basic calibration steps (e.g. bias correction, flat fielding, image crosstalk correction) and we use the ASTROMATIC¹ software suite (SOURCE EXTRACTOR, hereafter SE, v.2.19.5; SCAMP, v.2.0.1; SWARP, v.2.38.0; Bertin & Arnouts 1996; Bertin et al. 2002; Bertin 2006) to perform the astrometric

¹ <http://www.astromatic.net/software>

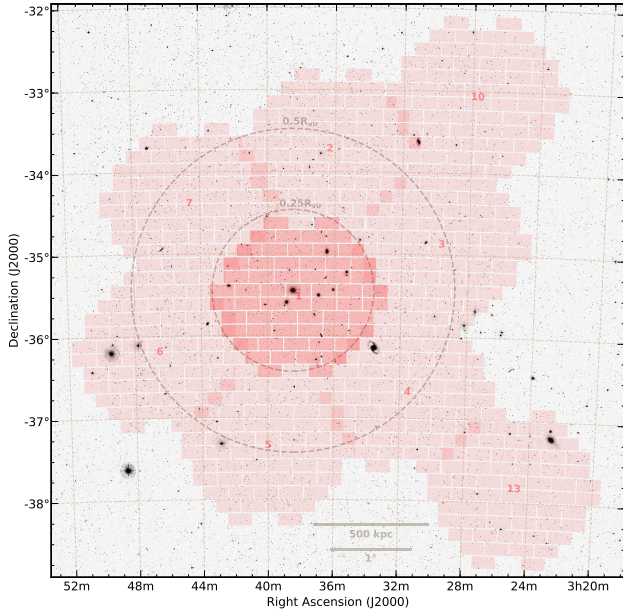


FIG. 1.— Overview of the NGFS mosaic footprint consisting of DECam tiles 1–7, 10, and 13, with the central tile investigated in this work, being highlighted. The dashed circles indicate a quarter and a half virial radius, i.e. $0.25 R_{\text{vir}}$ and $0.5 R_{\text{vir}}$. The underlying figure is taken from DSS1 obtained via the Online Digitized Sky Surveys server at the ESO Archive. The displayed field is $7^\circ \times 7^\circ$.

and photometric calibrations based on reference stars from the 2MASS Point Source Catalog (Skrutskie et al. 2006) and SDSS stripe 82 standard star frames, respectively, to build our image stacks. We then apply our custom background subtraction strategy based on an iterative masking and sky modeling procedure. We cross-validated our $u'g'i'$ photometry by running PSF photometry in the surveyed area and comparing the resulting magnitudes with the U, B, V and I photometry of Kim et al. (2013) for globular clusters in the same field. In order to adequately compare the two photometries we utilized the empirical transformation equations from Jordi et al. (2006) and found good agreement within the uncertainties.

In a previous contribution (Muñoz et al. 2015), we presented a preliminary i' -band based analysis of a rich population of dwarf galaxies in the central $\sim 3 \text{ deg}^2$ tile of the NGFS footprint. Here we build upon these results by including the full $u'g'i'$ color information for the central dwarf galaxy population with an average seeing of $1.7''$ in u' , $1.3''$ in g' , and $1.1''$ in i' . In order to evaluate the detection threshold for extended sources in u' , g' , and i' , we directly measured the pixel statistics on the sky in the individual passbands, resulting in $1-\sigma$ surface-brightness limits of $\mu_{u'} = 28.04$, $\mu_{g'} = 29.06$, and $\mu_{i'} = 28.15$. Figure 2 illustrates the footprint of the central NGFS tile.

3. ANALYSIS

3.1. Detection of LSB dwarf galaxies

To detect LSB dwarf galaxy candidates we first constructed RGB images from the observed $u'g'i'$ frames to take advantage of the total flux captured in each passband while preserving color information. We then visually inspected these frames looking explicitly for diffuse LSB galaxies. The RGB images allow us to easily identify dwarf galaxy candidates by considering their colors, sizes, and overall morphologies (e.g. comparatively flat surface brightness profile and nucle-

ation). We also included LSB galaxies having SF knots and/or blue colours, not specifically selecting against these sources. While automated algorithms can prove very effective in detecting faint galaxies (NGVS paper, Ferrarese et al, 2017, ApJ, in press), for the purpose of this work, we present a by-eye classification done independently by several people. The advantage of this method over automated algorithms like SE is obvious. For example, SE is only able to analyze one frame–passband combination at a time and often fails to detect extended LSB sources due to contamination by foreground stars, while visual inspection allows for the identification of galaxy candidates based on all aforementioned criteria simultaneously. We find that galaxy color is particularly effective in this regard since the colors of cluster dwarfs are expected to follow a cluster red sequence as seen in many galaxy aggregates (Gladders & Yee 2005; Roediger et al. 2017), with likely origins in the galaxy mass-metallicity relation. Combining this criterion with the diffuse morphologies arising from shallow dwarf surface-brightness profiles results in a straight-forward detection strategy for dwarf galaxy candidates. Despite these advantages, the disadvantage of visual inspection is that it precludes us from quantifying a selection function to verify sample completeness and that it has the potential to introduce human bias. Hence, to avoid any personal detection biases, we (PE, THP, YO, MAT, KAM, KXR) individually investigated the RGB images independently, yielding up to six separate dwarf galaxy candidate catalogues for each tile. Tile 1 has five independent candidate catalogues.

3.2. Quality flags

To estimate the reliability of our detections we match the catalogues using TOPCAT (Taylor 2005) to quantify in how many catalogues a given source was found. We then assign quality flags to each dwarf galaxy candidate such that one found in all five catalogues is assigned a flag \mathcal{A} , in four catalogues a flag \mathcal{B} , and so on. The matching is done systematically so that we first match all flag \mathcal{A} objects, and remove them from the corresponding catalogues. We continue by searching for flag \mathcal{B} sources, and continue until all remaining sources are flag \mathcal{E} , i.e. untrustworthy candidates only identified by a single team member. In order to find all matches for a given flag k , all possible $\binom{5}{k}$ catalogue combinations have to be matched, leading to lists of 145 flag \mathcal{A} , 59 flag \mathcal{B} , 54 flag \mathcal{C} , 29 flag \mathcal{D} , and 136 flag \mathcal{E} sources.

Figure 3 shows the distribution of quality flags, which illustrates the potential human detection bias given the large number of accumulated flag \mathcal{E} sources present in the merged candidate catalogue. Conversely, those sources with multiple independent identifications, i.e. flags $\mathcal{A}\mathcal{B}\mathcal{C}\mathcal{D}$, show a strong trend toward unanimous detections. Flags \mathcal{E} illustrate the average number of sources uniquely identified by one person (solid line) as well as all accumulated sources (dashed line).

The lower panel in Figure 3 shows the correlation between detection flags and median values of galaxy apparent g' -band magnitude, effective radius (r_e), and surface brightness ($\mu_{g'}$) for each flag. As expected, apparent magnitude and r_e show clear trends toward brighter/larger galaxies having flags \mathcal{A}/\mathcal{B} , while flags \mathcal{D}/\mathcal{E} correspond to fainter/smaller sources. No obvious correlation is seen with $\mu_{g'}$. We note that these correlations should be taken with caution, since we only measure structural parameters for a small subsample of $\mathcal{D}\mathcal{E}$ flags. Moving forward, we consider only galaxies with detection

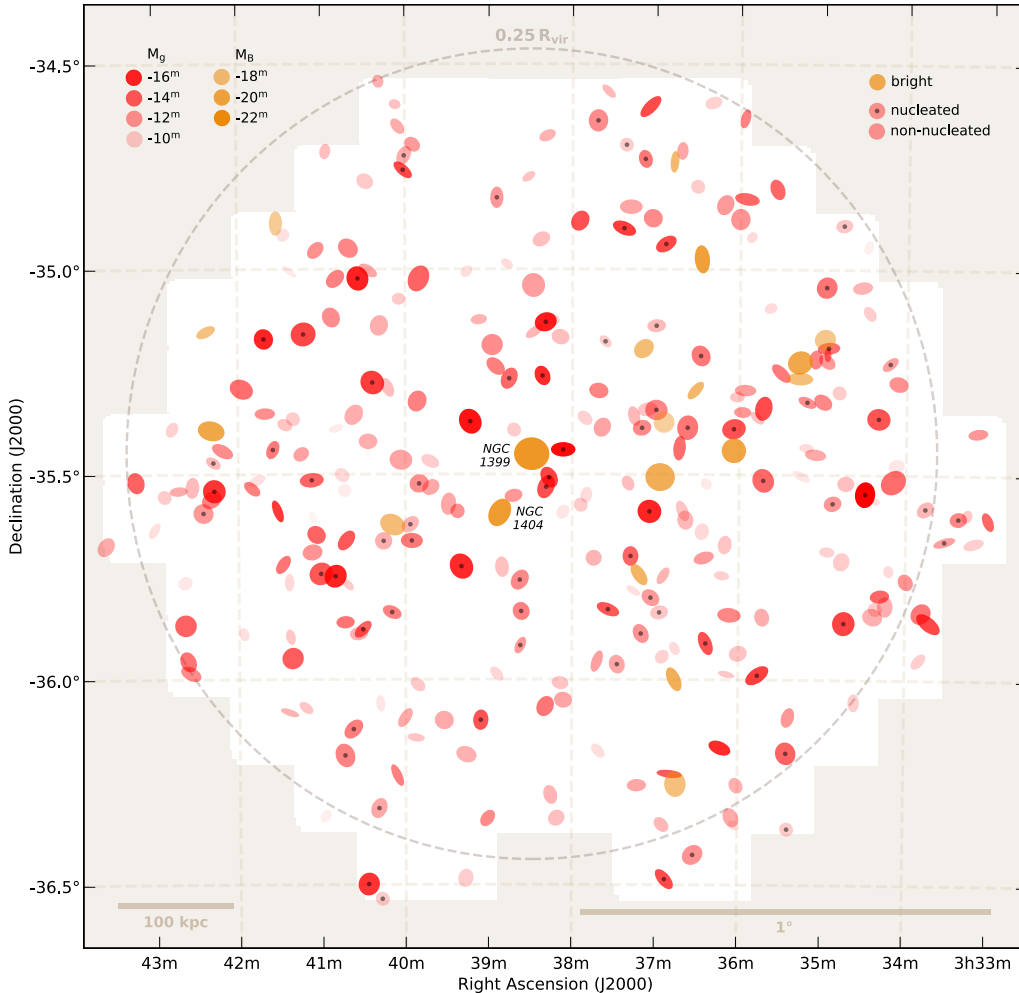


FIG. 2.— Spatial footprint of the central NGFS tile centered on NGC 1399 and analyzed in this paper (shown in white). The distribution of the dwarf galaxy population corresponds to the one listed in Table 1. Both bright galaxies ($M_B \leq -16$; orange) and dwarfs (red) are indicated, and the two brightest galaxies are labeled with their NGC numbers. Ellipticities and position angles of the symbols are scaled by the corresponding GALFIT model values. The dashed circle indicates $0.25R_{\text{vir}}$ of the Fornax cluster ($R_{\text{vir}} = 1.4$ Mpc), as determined by Drinkwater et al. (2001).

flags \mathcal{ABC} , i.e. at least three independent identifications to be dwarf galaxy candidates, yielding a final sample of 258 sources. Of these candidates, 75 ($\sim 29\%$) show evidence of nucleation based on visual inspection of the u' , g' , and i' -band images, while 183 galaxies ($\sim 71\%$) show no nucleus.

3.3. Comparison with existing catalogues

We compare our sample with galaxies flagged as *likely members* in the Fornax Cluster Catalogue (FCC Ferguson 1989). Out of 340 FCC galaxies, 112 fall in our observed DECAM footprint. We note that we could not re-identify FCC 162, which is reported to be located within the halo of the bright elliptical NGC 1379 (FCC 161), leaving 111 recovered FCC galaxies. Of these, 90 are fainter than $M_B = -16$ mag and, hence, can be considered as dwarf galaxies (Ferguson & Bingeli 1994; Tammann 1994). In addition, two galaxies with $M_B \lesssim -16$ (FCC 136 and FCC 202) have explicitly been classified as dwarfs in the FCC catalogue, resulting in a total number of 92 FCC dwarfs in our observed footprint. We also recover 45 galaxies from the Mieske et al. (2007) catalogue that have not been classified as FCC galaxies. Finally, we checked for Mieske et al. (2007) dwarfs that are not in

our sample and conclude that, based on their morphologies and colors, all are likely to be background galaxies. Summarizing, we find a sample of $258 - 92 - 45 = 121$ previously uncatalogued dwarf candidates. We note that this number is smaller than in our recent publication (see Muñoz et al. 2015), since in the present work we only consider galaxies with quality flags \mathcal{ABC} as dwarf identifications.

Figure 2 shows a schematic representation of the spatial distribution of the detected dwarf galaxy candidates and known bright galaxies in the central DECAM tile of the NGFS footprint analyzed in this work (tile 1 in Fig. 1). The symbol shape, alignment, size, and opacity of each galaxy marked in Figure 2 is scaled by the corresponding ϵ , PA, r_e , and M_i , respectively, as obtained from our GALFIT models. We point out that since precise 3D spatial information is not known, M_g may vary by up to ~ 0.16 mag due to the unknown depth of the cluster².

3.4. Surface Brightness Profile Modeling

² This applies only under the assumption of spherical symmetry.

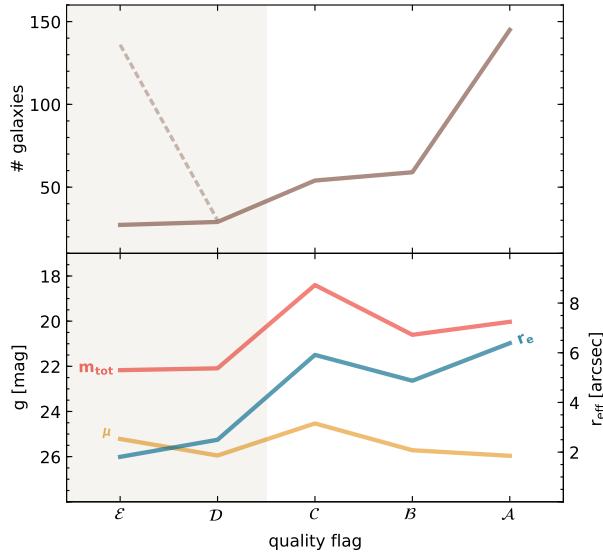


FIG. 3.— Dwarf galaxy candidate detection flags. *Upper panel:* Distribution of detected dwarf galaxy candidates as a function of the quality flags. For flags \mathcal{E} the solid line indicates the average number of sources uniquely identified by one person, while the dashed line shows all accumulated flag \mathcal{E} objects. *Lower panel:* Total galaxy magnitudes (red), surface brightness (yellow), and effective radii (blue) as a function of quality flags. Sources with flags \mathcal{ABC} are considered dwarf galaxy candidate detections. See text for details.

We determine the structural parameters for the 258 dwarf candidates in u' , g' , and i' filters utilizing the software package GALFIT (v3.0.5; Peng et al. 2010). GALFIT is an effective tool for extracting structural information of dwarf galaxies, allowing the user to model the two-dimensional distribution of the diffuse starlight in galaxies with numerous parametric functions. Utilizing the full 2D information for a given galaxy enables us to obtain reliable fits to the surface-brightness distribution constrained by each non-masked image pixel. Surface-brightness profiles of dwarf galaxies are commonly well-fit by a single-component Sérsic (1968) model

$$I(r) = I_e \exp\{-b_n[(r/r_e)^{1/n} - 1]\} \quad (1)$$

which is parametrized by the effective radius r_e , the intensity I_e at r_e , and the shape index n (also referred to as the Sérsic index) that defines the curvature of the model. The parameter b_n is linked to n such that half of the total light from the model is enclosed within r_e (Caon et al. 1993). We choose this single component, ellipsoidal model to measure the global morphology of our dwarf galaxy candidates.

Our iterative fitting procedure is split into several steps. First we create postage stamp images for each dwarf candidate in the u' -, g' -, and i' -band frames and construct corresponding segmentation maps using SE. The segmentation maps are used to create bad-pixel masks for each dwarf, masking any non-dwarf sources above a 2σ threshold. This initial step results in dwarf-only images that are used for subsequent model fits.

3.4.1. Automatic and Refined Fitting

In a first iteration we fit galaxies assuming four different initial guesses for the Sérsic model parameters. By comparison between the four resulting model fits for each galaxy we ob-

tain a qualitative estimate of the robustness of a fit. In the best scenario, all initial guesses converge to the same solution, but in most cases two or three initial guesses converge to a single model, leaving one or two outliers. In the worst cases, all initial guesses yield different results. To properly assess the reliability of the fits, we compare the galaxy, model, and residual images for each dwarf in detail. In most cases where multiple initial guesses converge to the same result, visual inspection shows the fits to be reliable.

In the second iteration we consider galaxies for which the automatic fitting procedure did not converge to a common solution due to their diffuse natures and/or small extents. For these galaxies — the majority of our sample — the models display a severe mismatch with respect to the surface-brightness distributions of the galaxies, or the residual images show signs of over-subtraction. We refine the fitting procedure for these galaxies as follows.

First, we estimate the total galaxy luminosity by running SE on the galaxy postage stamp images and use the resulting MAG_AUTO values from the corresponding segmentation as initial guesses for the GALFIT Sérsic models. Keeping these values fixed reduces the number of free parameters available for the next galaxy model, stabilizing the fit and resulting in more robust estimates of the remaining model parameters. We then use the new parameters and fix them and allow GALFIT to recompute the galaxy luminosity freely. In the final step, the newly determined galaxy magnitude was again fixed, and we recompute the other parameters resulting in model parameters that are all consistently derived by GALFIT. In this way, all non-nucleated dwarfs are fit successfully, leaving little to no sign of the galaxies' light in the residual images (see Fig. 4).

3.4.2. Fitting Nucleated Dwarfs

We modify the above strategy for dwarf candidates that show evidence of nucleation in order to account for the excess light at their centers. While in principle a two-component model consisting of a King (1962) profile for the nucleus and a Sérsic profile for the spheroid would be preferred, the pixel-scale sizes of the nuclei preclude this approach. Very few stable solutions are found for the nuclei, and the addition of model parameters increases the likelihood of degenerate solutions, making this approach futile.

As a solution to this problem, for a given nucleated candidate, we instead mask the nucleus and fit a single Sérsic model to the diffuse spheroid iteratively. We first manually create a preliminary mask for the nucleus in the segmentation maps and use it to fit the galaxy light without the nuclear component. From the resultant residual images (including the nucleus) we generate an improved mask for the nucleus and any other sources contaminating the diffuse components of the dwarfs. We then repeat the fit using the improved mask, and iteratively improve the mask and residual image. If the nucleus is not masked correctly, the Sérsic model will attempt to fit it partially, thus predicting a too high n , and producing symmetric regions of over- and under-subtraction in the residuals. Following this procedure, we find that three to four iterations result in clear nucleus-spheroid separation free of symmetric residuals in the circum-nuclear regions, and give stable solutions for the spheroid components of all nucleated dwarf candidates confirmed by visual inspection.

Figure 4 shows models for eight (four non-nucleated and four nucleated) representative dwarf galaxies with successively decreasing average surface-brightness in the range $24.0 \lesssim \mu_{i'} / \text{mag} \lesssim 26.5$. Comparison of the galaxies (top row),

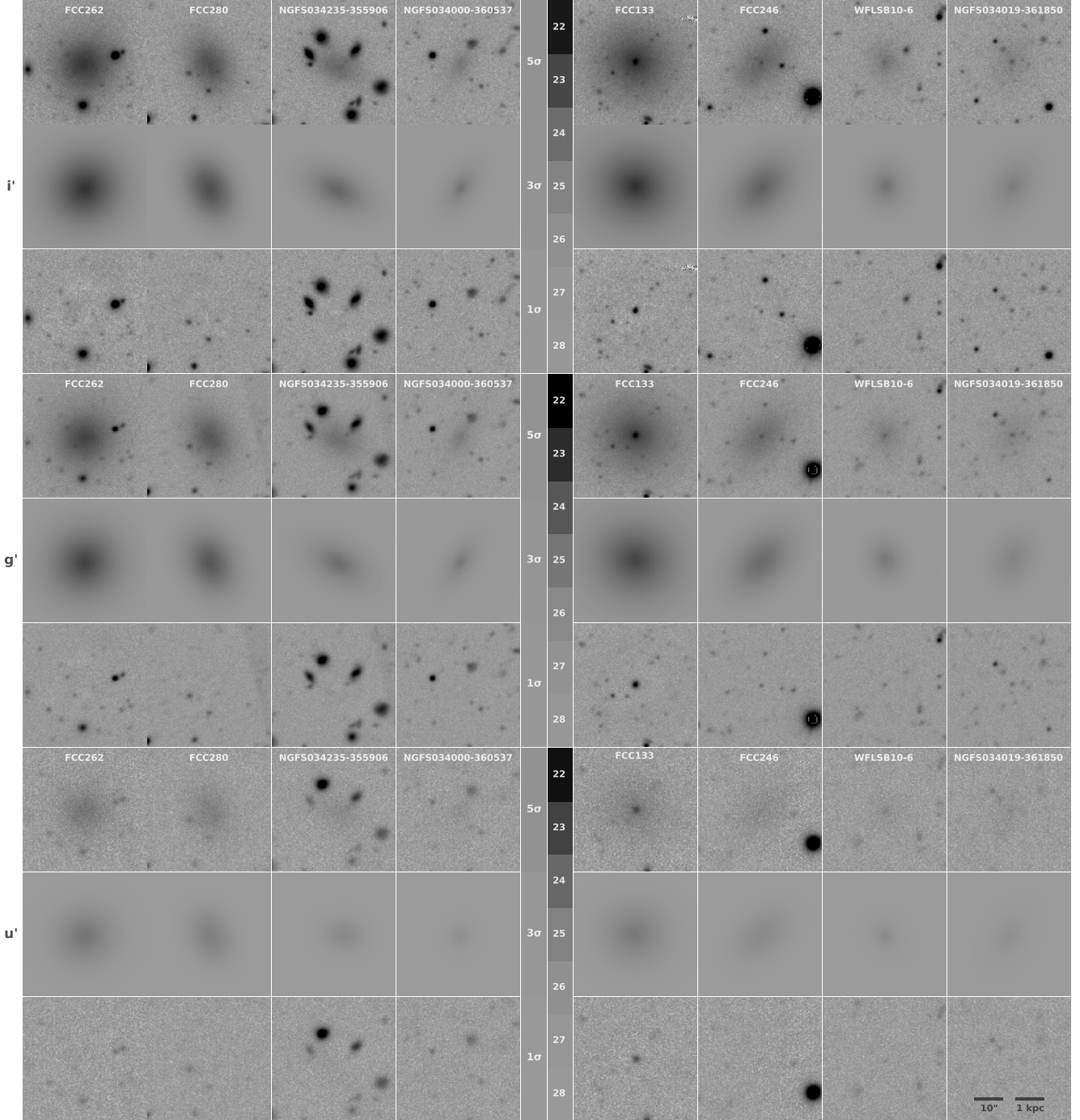


FIG. 4.— Examples of the dwarf galaxy surface-brightness modeling with GALFIT. Four non-nucleated (left) and four nucleated (right) dwarfs with successively decreasing (left to right) effective surface brightness values are shown in u' (lower panels), g' (middle panels), and i' (upper panels) as examples. We show the dwarf galaxy postage stamps, the corresponding 2D Sérsic (1968) models and residual images (galaxy–model) for every passband. The greyscales show values of constant surface brightness ranging from $\mu = 22$ to 28 mag arcsec $^{-2}$ in steps of 1 mag arcsec $^{-2}$ as well as 1σ , 3σ , and 5σ surface-brightness detection thresholds in all passbands. Note that only the spheroid component is modelled for nucleated dwarfs so that the nuclear star cluster is visible in the residual images. We also point out the clear variance in the nucleus-to-galaxy luminosity ratio for these dwarfs. Dwarfs are f.l.t.r.: FCC262, FCC280, NGFS034235-355906, NGFS034000-360537, FCC133, FCC246, WFLSB10-6, NGFS034019-361850. The images cover $0.72'$ (~ 4.25 kpc) on a side.

models (middle row), and residuals (bottom row) clearly illustrates the robustness of our modeling approach. In total, we derive structural properties for 246/258 (95%) of the detected dwarf candidates in i' - and g' -bands, dropping to 144 (56%) in the u' -band. While the lower fraction of modeled galaxies in the u' -band is likely due to lower sensitivity and compar-

tively low flux of galaxies in this particular passband, the 12 missing galaxies in the i' - and g' -bands are either too faint, or too strongly contaminated by a bright nearby star. We list our photometric results in Table 1, including galaxy coordinates, all available total galaxy magnitudes derived from GALFIT, integrated galaxy colors, absolute g' -band magnitudes ($M_{g'}$),

and estimated total stellar masses (\mathcal{M}_* ; see also § 4.3). We also list the cross-identifications from the FCC and the Mieske et al. (2007) catalogues. Likewise, we list in Table 2 all available structural parameters derived by GALFIT in this work, also indicating for each galaxy whether or not a nucleus is present.

4. RESULTS

4.1. Structural Parameters

We show in Figure 5 the distribution functions of the structural parameters derived by GALFIT for the entire dwarf galaxy sample in the u' , g' and i' -filters. The upper panels show the distributions of effective radius (r_e), Sérsic profile shape parameter (n), ellipticity (ϵ), and the position angle (PA), split by filter with u' in the top row followed by g' and i' below. The histogram bin-widths were chosen based on Knuth's rule (Knuth 2006). Alternative visualizations of the distributions are shown by the solid relations, which are non-parametric *Epanechnikov*-kernel probability density estimates (KDEs) for each parameter-filter combination. The lower panels show consistency plots for each structural parameter, as derived from the u' , g' and i' -filter.

While r_e and n show well-defined peaks in their distributions, the ϵ and PA values are more broadly distributed. We find a characteristic effective radius consistent between the passbands in the range $0.1 \leq r_e/\text{kpc} \leq 2.0$ with a similar mean size of $\langle r_e \rangle_{g'} = 0.68 \pm 0.02$ kpc, $\langle r_e \rangle_{i'} = 0.71 \pm 0.03$ kpc, and $\langle r_e \rangle_{u'} = 0.69 \pm 0.03$ kpc, which is at first impression indicative of a lack of significant stellar population gradients in the spheroid components. We find in all filters similar minimum drop-offs in r_e and similar $r_{e,\text{max}} \approx 2$ kpc. However, the r_e consistency plots in the bottom panels show that the u' -band half-light radii are systematically smaller than in the redder bands. This may be due to the lower surface-brightness depth of our u' -band data and/or stellar population gradients pointing towards bluer cores of dwarf galaxy spheroids. Quantitatively evaluating the detailed causes of this intriguing result goes beyond the scope of this paper. We will, however, return to this aspect in a future paper on the stellar population content of the NGFS dwarf galaxies. The distributions of Sérsic indices n closely follow Gaussian profiles in all passbands with similar mean values of $\langle n \rangle_{u'} = 0.83 \pm 0.03$, $\langle n \rangle_{g'} = 0.78 \pm 0.02$, and $\langle n \rangle_{i'} = 0.83 \pm 0.02$. However, we note that there may be an observational bias giving rise to the narrow distributions in n , likely due to selection effects since we explicitly looked for diffuse galaxies in our search for dwarf galaxy candidates.

We find generally more platykurtic distributions in ϵ and PA than in r_e and n . Our measurement values range between $0.0 \lesssim \epsilon \lesssim 0.7$, with indications that ϵ may be bimodally distributed. Despite the visual impression, detailed Gaussian mixture modeling (GMM) does not conclusively quantify whether a single-mode or a bimodal distribution is preferred. We find a marginal tendency of increasing average ellipticity towards bluer passbands.

Interestingly, we do not find any highly elongated dwarfs, with 97% of the NGFS dwarfs exhibiting ellipticities $\epsilon < 0.55$. This is in very good agreement with the result from Sánchez-Janssen et al. (2016) for dwarfs in the core of the Virgo cluster, and with the fast rotators in the ATLAS3D sample (Cappellari 2016). Finally, we see that position angles do not show any preferred alignment and populate the whole parameter range $0^\circ \lesssim \text{PA} \lesssim 180^\circ$ with very good consistency between the u' ,

g' and i' -filter.

The lower panels in Figure 5 compare the derived structural parameters in all three passbands. Assuming the galaxies are homologous in all passbands, i.e. same r_e , n , ϵ , and PA, one would expect all galaxies to follow unity, with the observed scatter arising from the statistical uncertainties of the measurements. However, this would also imply that the dwarf candidates do not exhibit color gradients, which is not necessarily true, as pointed out above. Hence, while the statistical measurement errors likely contribute to the observed scatter, intrinsic differences between galaxy models – e.g. color gradients – may also play a role. In general, the i' vs. u' -band comparison shows a systematically larger scatter than that of the i' vs. g' -bands, in part likely due to the shallower u' -band observations. Detailed consideration of the derived R^2 values reveals that r_e and PA show the tightest correlations, implying that these structural parameters constrain the galaxy models most efficiently in either of the filters. Meanwhile, the n distribution shows a much larger deviation from unity, indicating that it is more difficult for GALFIT to find one unique solution for the Sérsic index in all passbands. In any case, we note that the range in n is relatively small, i.e. 83% of the measured galaxies have shape parameters in the range $0.5 \lesssim n \lesssim 1.5$, and variations on the order of $\Delta n \approx 0.1$ are expected.

We also highlight the nucleated dwarfs in the parameter distributions of the upper panels of Figure 5, which clearly show that the average spheroid of a nucleated dwarf has a larger half-light radius and more spherical light distribution, with a hint of a slightly more exponential-type Sérsic profile (i.e. n closer to 1) than their average non-nucleated counterpart. There is mild indication that the spheroid components of nucleated dwarf galaxies are more spheroidal, i.e. show lower ellipticity, than their non-nucleated counterparts. Except for effective radii, the nucleated dwarf samples show tighter correlations than the overall samples in the filter correlation plots. This is primarily due to the fact that nucleated dwarfs are on average brighter than non-nucleated dwarfs. We find that the nucleation fraction (\mathcal{F}_{nuc}) is a strong function of galaxy luminosity. \mathcal{F}_{nuc} shows a strong tendency towards higher fractions in bins containing the brightest galaxies, and declines to $\sim 0\%$ when only the faintest galaxies are considered. Likewise, the cumulative \mathcal{F}_{nuc} shows a similar trend, in that $\mathcal{F}_{\text{nuc}} = 100\%$ for exclusively bright galaxies, and falls to the final value of $\sim 29\%$ for the overall dwarf galaxy sample. The same trend of higher nucleation fractions in brighter dEs was found in the Virgo cluster by Grant et al. (2005) and Lisker et al. (2007), indicating a possibly, generally valid trend. We furthermore note that, given the present seeing, low-luminosity nuclei that have low contrast with the host galaxy could remain unidentified and affect the derived nucleation fraction.

4.2. Color-Magnitude Relations

Color-magnitude diagrams (CMDs) of galaxies have long been used to infer the mass assembly and star formation histories of galaxies in large-area, deep surveys with ground and space-based telescopes (e.g. Baldry et al. 2004; Bell et al. 2004, 2012; Faber et al. 2007; Trayford et al. 2016; Roediger et al. 2017). Multi-passband CMDs are powerful tools to obtain constraints of luminosity-weighted average stellar population ages and metallicities, as well as stellar masses of large samples of galaxies (e.g. Chilingarian & Zolotukhin 2012).

In the left panels of Figure 6 we show the $(g'-i')_0$, $(u'-g')_0$, and $(u'-i')_0$ vs. g' CMDs for NGFS dwarf galaxies and compare them with other galaxy samples and theoretical pre-

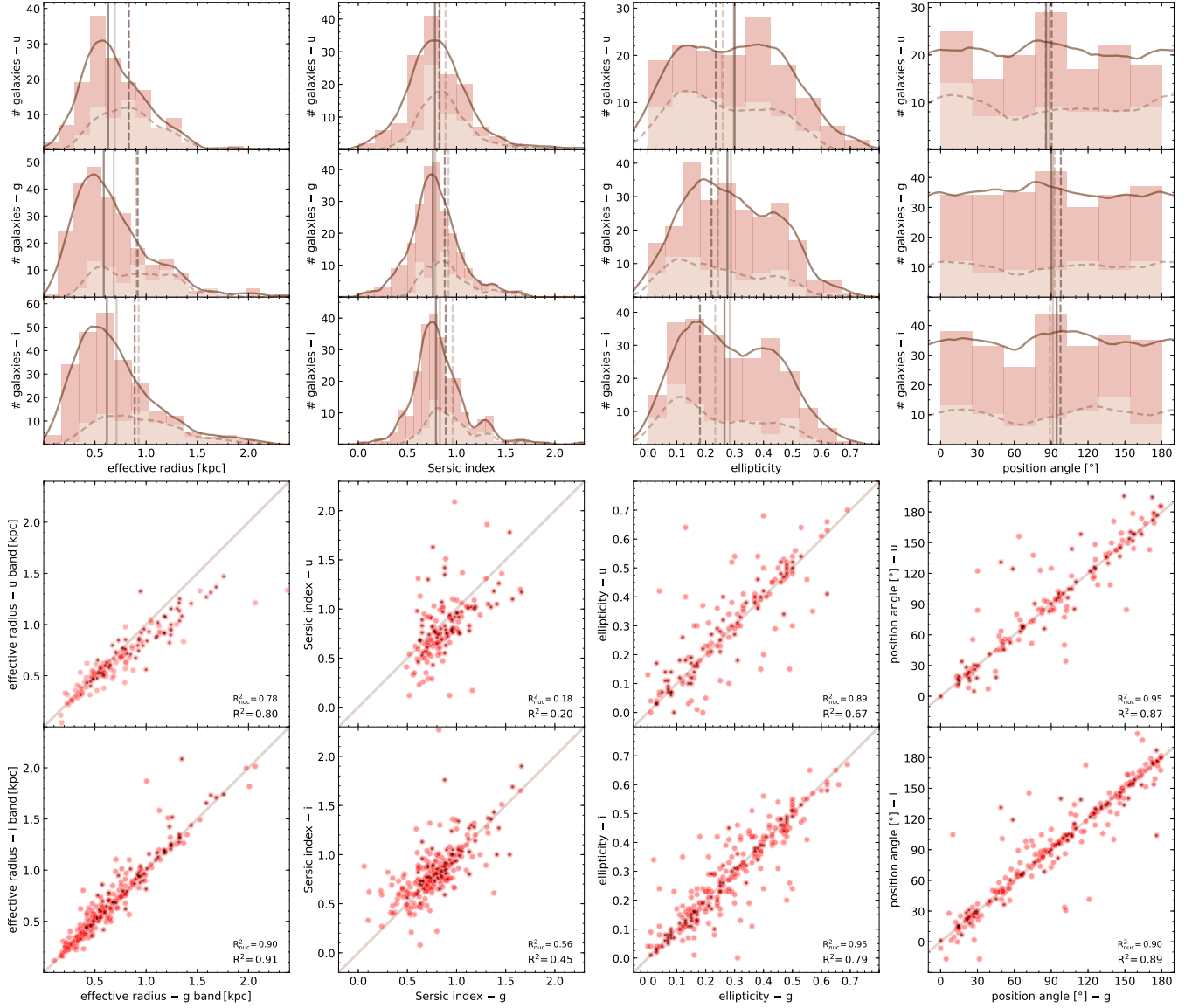


FIG. 5.— Structural parameters derived from GALFIT in the u' , g' , and i' filters. *Upper panels*: the distributions for the effective radius (r_e), Sérsic profile shape parameter (n), ellipticity (ϵ), and the position angle (PA) in all three passbands. Lighter histograms refer to nucleated dwarfs only. Smooth curves show the corresponding Epanechnikov-kernel probability density estimates for the entire sample (solid) and nucleated dwarfs only (dashed). Vertical lines indicate the mean (lighter) and median (darker) of the overall distributions for the entire sample of dwarf galaxies (solid lines) and nucleated dwarf only (dashed lines). *Lower panels*: the comparison of u' - and g' -band parameters as a function of the corresponding i' -band values. Straight lines show the unity relations. Symbols with black dots refer to nucleated dwarfs. Correlation coefficients R^2 are shown in each panel for both the overall sample and the nucleated dwarfs only.

dictions of color-magnitude relations. We account for foreground extinction toward Fornax by utilizing average extinction coefficients ($A_{u'}$, $A_{g'}$, and $A_{i'}$) derived from several bright Fornax galaxies based on the re-calibrated extinction maps of Schlafly & Finkbeiner (2011), noting that the extinction variance across the observed field is $\sigma_{A_{u'}} \simeq 0.008$, $\sigma_{A_{g'}} \simeq 0.006$, and $\sigma_{A_{i'}} \simeq 0.003$ mag. Dashed lines show the iso- M_* relations based on the Bell et al. (2003) color- M/L conversions (see also Sect. 4.3). Given the photometric limits of the combined dataset the sample reaches down to stellar masses $\sim 10^6 M_\odot$, while the optical g' and i' -band photometry reaches even lower values. All three panels clearly illustrate the expected red sequence for early-type cluster galaxies, where brighter systems exhibit redder colors than fainter ones. This color-magnitude relation of galaxies is commonly interpreted as a mass-metallicity relation since the deeper po-

tential wells of more massive galaxies more easily retain metals produced throughout their star-formation history (e.g. Kodama & Arimoto 1997; Poggianti et al. 2001; Tremonti et al. 2004; Savaglio et al. 2005; Maiolino et al. 2008; Baldry et al. 2008; Møller et al. 2013; Segers et al. 2016; Ma et al. 2016).

We fit linear relations to the CMDs of NGFS dwarfs and derive shallow color gradients in the sense of $\Delta(g' - i')_0 / \Delta g' = \nabla_{(g'-i')_0} = -0.01$, $\Delta(u' - g')_0 / \Delta g' = \nabla_{(u'-g')_0} = -0.09$, and $\Delta(u' - i')_0 / \Delta g' = \nabla_{(u'-i')_0} = -0.13$.

We note that the scatter present around the red sequence likely arises from effects intrinsic to the constituent stellar populations (e.g. spreads in ages/metallicities) and/or from photometric uncertainties. To quantify the scatter in the observed CMDs we computed the variance of the measured values with respect to the linear fits, obtaining $\sigma_{(g'-i')_0} = 0.25$, $\sigma_{(u'-g')_0} = 0.24$, and $\sigma_{(u'-i')_0} = 0.27$ mag. We discuss below

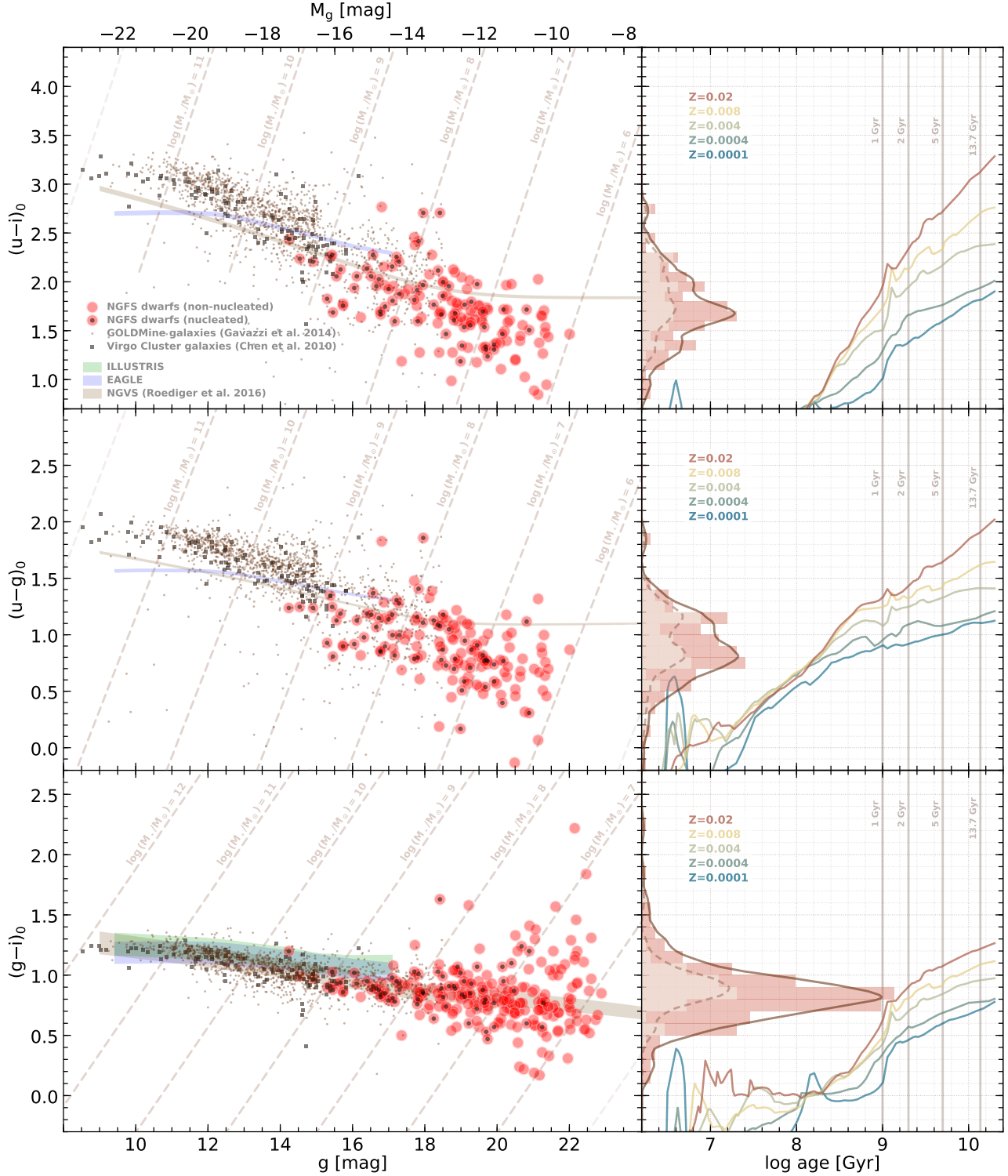


FIG. 6.— Color-magnitude diagrams and simple stellar population model predictions for stellar populations in NGFS galaxies. *Left panels:* Color-magnitude relations based on u' , g' , and i' -band photometry. Dashed lines show M_* estimates from Bell et al. (2003), while solid lines show red sequence fits from NGVS (Roediger et al. 2017). *Right panels:* Color distributions are shown along the ordinate of each panel for both the overall (dark shading) and nucleated dwarfs (light shading) samples. Also overlaid are Bruzual & Charlot (2003) model predictions relating SSP ages and metallicities with the corresponding galaxy colors. Vertical lines indicate ages at 1, 2, 5, and 13.7 Gyr.

(see Sect. 4.2.3) the implications of these color variances in terms of stellar population properties.

4.2.1. Comparison with other Environments

In order to put our Fornax measurements in a larger context, we overplot in Figure 6 the red-sequence fits for Virgo cluster galaxies from the NGVS (see Roediger et al. 2017). This dataset is comparable to our NGFS data in photometric depth, SED sampling and homogeneity. For this, we convert the NGVS photometry to the standard SDSS system utilizing the photometric transformation equations on the CADC website³. The brown shaded area illustrates the uncertainty in the photometric transformation arising from multiple transformation equations and filter throughput mismatch. We also plot earlier CMD relations for the 100 ACS Virgo Cluster Survey (ACSVCS) galaxies based on SDSS measurements (Chen et al. 2010). In addition, we show measurements from the GOLDMine database (Gavazzi et al. 2003, 2014) for various other environments, including the Coma, Cancer, Hercules, A2197, and A2199 galaxy clusters, as well as the Local Supercluster.

With the combined empirical dataset, we note a relatively sharp red cutoff for galaxies at the upper envelope of the red sequence in the $(g' - i')_0$ vs. g' CMD, which continues from bright galaxies with $10^{11} M_\odot$ down to faint luminosities of our NGFS dwarf galaxy sample at $10^7 M_\odot$ and lower masses. Galaxies above this threshold are potentially heavily reddened or possible background sources, and their offsets from the red sequence toward redder colors are even more obvious in the $(u' - g')_0$ and $(u' - i')_0$ CMDs, likely a result of internal dust absorption and/or redshift in combination with the wider SED sampling.

We note that the NGVS red sequence fit lies systematically towards redder colors compared to the present NGFS $(u' - g')_0$ and $(u' - i')_0$ data. Despite the photometric filter transformation uncertainties, one might speculate whether this discrepancy is due to a systematically lower metallicity of the dwarf galaxy population in Fornax compared to Virgo. But we defer further discussion on this interesting aspect until spectroscopic metallicities become available.

4.2.2. Comparison with Numerical Model Predictions

In order to test whether the overall empirical datasets shown here are in agreement with current galaxy formation models, we overplot theoretical color-magnitude red-sequence predictions from the Illustris and EAGLE simulations (Vogelsberger et al. 2014; Schaye et al. 2015). Illustris consists of eight cosmological N-body hydrodynamic simulations, each spanning a volume of $\sim 10^6 \text{ Mpc}^3$, differing in terms of resolution, among other things, while EAGLE comprises six simulations similar to Illustris, running a modified SPH code. In order to ensure a consistent comparison between these simulations, our dataset, and the NGVS red-sequence fits we utilize the same model relations as shown in Roediger et al. (2017), i.e. adopting the same selection criteria for obtaining the samples of Illustris and EAGLE galaxies. The galaxy populations from both numerical models cover a range of $\mathcal{M}_* \gtrsim 10^{8.5} M_\odot$ while our NGFS dwarf sample reaches masses down to $\mathcal{M}_* \gtrsim 10^6 M_\odot$. The green and blue-shaded bands illustrate the uncertainty in the photometric transformation from NGVS photometry to the standard SDSS system. Both the Illustris and

EAGLE simulations predict systematically redder colors than the NGFS dataset and the NGVS fits for galaxies fainter than $M_{g'} \approx -18 \text{ mag}$ ($\sim 10^{10} M_\odot$). We observe that no model reproduces the red sequence slope in Fornax' and Virgo's core (see Roediger et al. 2017), with model slopes being systematically shallower than observed. We conclude that this discrepancy could be explained by shortcomings of the galaxy formation models. Unfortunately, given the small overlap in mass between these models and the NGFS dataset, a statistically robust comparison between the red-sequence model slopes and the present data is not feasible.

4.2.3. Stellar Population Properties

The right-hand panels of Figure 6 show an attempt to constrain the (luminosity-weighted) ages of the dwarf candidate sample by comparing their broad-band colors with the prediction of simple stellar population (SSP) models of Bruzual & Charlot (2003)⁴, hereafter BC03. These models provide color predictions for Chabrier (2003), Kroupa (2001), and Salpeter (1955) stellar initial mass functions (IMFs) using BaSeL (Westera et al. 2002), STELIB (Le Borgne et al. 2003), and MILES (Sánchez-Blázquez et al. 2006) stellar libraries. We compare the various SSP permutations for $(g' - i')_0$, $(u' - g')_0$, and $(u' - i')_0$ colors, finding that changing IMFs has minimal effect on the predicted galaxy colors (average of maximum deviations in all colors and metallicities is of order $\sim 0.02 \text{ mag}$), while switching stellar libraries results in more significant, but still minor differences (average of maximum deviations in all colors and metallicities is $\sim 0.10 \text{ mag}$). See Powalka et al. (2016) for more comparisons between model predictions. In the following we utilize the BC03 models based on the MILES stellar library with a Chabrier IMF.

We further explore the color distributions with the histograms and associated Epanechnikov-KDEs shown along the ordinates in the right panels of Figure 6, for both the overall (red shading) and nucleated (light shading) samples. While the overall population shows generally symmetric color distributions about the peaks, the nucleated subsample exhibits a tendency towards redder average colors. This feature likely arises from the mass-metallicity relation, in light of the trend toward higher nucleation fractions with increasing luminosity shown in Figure 2 of Muñoz et al. (2015), and is consistent with similar findings for dwarf galaxies in the Virgo cluster (Grant et al. 2005).

We plot the BC03 SSP model predictions for metallicities in the range $0.0001 \leq Z \leq 0.02$ as a function of age. The models clearly demonstrate the well-known age-metallicity degeneracy that complicates stellar population studies based on broad-band optical colors. Nonetheless, relating our derived $(g' - i')_0$ colors with the BC03 tracks, we see that even at the highest metallicity ($Z = 0.02$), the average dwarf shows ages $\gtrsim 1 \text{ Gyr}$. Given the mass-metallicity relation for galaxies, it is likely that the vast majority of the low-luminosity dwarf sample have significantly lower metallicities. Kirby et al. (2013) measured spectroscopic metallicities from individual red-giant branch stars in fifteen MW dSphs, seven LG dIrrs, and thirteen M31 dSphs, finding that their metallicities scale as $\langle [\text{Fe}/\text{H}] \rangle = -1.69 + 0.30 \log(\mathcal{M}_*/10^6 M_\odot)$. Comparing this relation with metallicities of more massive galaxies from Gallazzi et al. (2005), Kirby et al. concluded that this relation is roughly continuous from the least massive systems at

³ <http://www.cadc-ccda.hia-ihp.nrc-cnrc.gc.ca/en/megapipeline/docs/filt.html>. We stress that that the transformation from the CFHT/MegaCam to the SDSS u -band is known to be biased, in the sense that the SDSS u -band covers substantially bluer wavelengths than the MegaCam u -band. Thus, the corresponding transformation between the filter sets becomes an extrapolation rather than an interpolation.

⁴ <http://www.bruzual.org/bc03/>

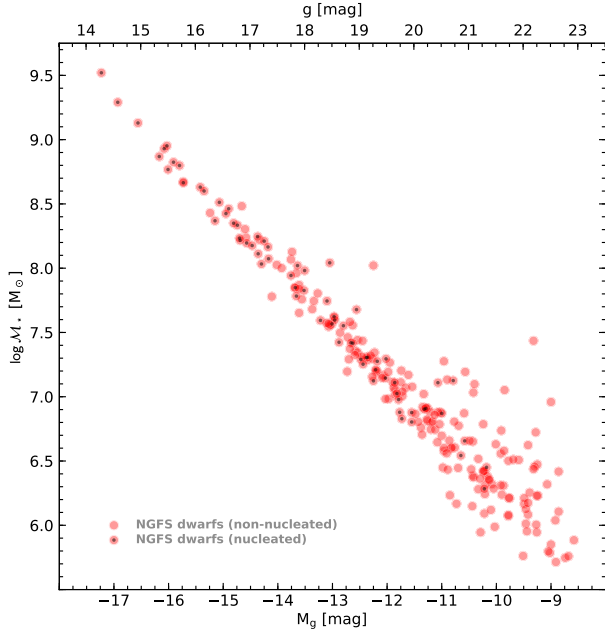


FIG. 7.— The stellar mass–luminosity relation for our sample dwarf galaxies. Stellar masses are estimated using the prescription of Bell et al. (2003) utilizing the derived and dereddened $(g'-i')_0$, $(u'-g')_0$, and $(u'-i')_0$ colors. Black dots denote nucleated dwarfs.

$\mathcal{M}_* = 10^{3.5} M_\odot$ to the most massive giant ellipticals at $\mathcal{M}_* = 10^{12} M_\odot$. Our most massive dwarf galaxy has $\log \mathcal{M}_* = 9.42$, corresponding to a metallicity of $[\text{Fe}/\text{H}] \approx -0.66$, if it follows the Kirby et al. (2013) relation. Considering standard abundances from Asplund et al. (2005), this converts to a metallicity of $Z \approx 0.003$. Hence, based on the BC03 model $(g'-i')_0$ model tracks, one can expect ages of at least 5 Gyr for the average dwarf in our NGFS sample. While showing the expected low metallicities, we note that the dwarf candidate sample exhibits a large spread in metallicity if it is mostly uniformly old, i.e. older than ~ 10 Gyr. This might be explained by the host cluster environment that is likely to have experienced epochs of significant chemical inhomogeneities and, hence, may have uniquely influenced the star formation histories of the individual galaxies. However, the difficulty in breaking the age–metallicity degeneracy with $u'g'i'$ photometry alone is obvious. Future imaging campaigns that sample different regions of the spectral energy distribution (e.g. Muñoz et al. 2014) and deep integrated-field spectroscopy (e.g. Mentz et al. 2016) will be very valuable in further constraining the stellar population properties of these low-mass NGFS galaxies to higher accuracy. We, thus, defer a more detailed stellar population analysis and a discussion of the build-up of the faint galaxy population (Boselli & Gavazzi 2014), including near-infrared photometry information, to future work.

4.3. Stellar masses

In order to study the physical scaling relations of the dwarf galaxy sample in relation with other stellar systems, we compute the stellar masses of our NGFS dwarf candidates using the prescriptions from Bell et al. (2003), which are good matches for the expected star formation histories of our NGFS spheroidal dwarf galaxies (Zhang et al. 2017). We parametrize the stellar mass-to-light ratios (\mathcal{M}_*/L_\odot) by

galaxy colors using the relation

$$\log(\mathcal{M}_*/L_\odot) = a_\lambda + b_\lambda \times \text{color} \quad (2)$$

where the coefficients a_λ and b_λ define the transformation for different filter combinations, i.e. colors (see Bell et al. 2003, their Table 7). We compute the g' and i' -band \mathcal{M}_*/L_\odot from our measured and de-reddened $(g'-i')_0$, $(u'-g')_0$, and $(u'-i')_0$ galaxy colors, yielding up to six \mathcal{M}_* estimates for a given galaxy. To compute \mathcal{M}_* , we derive galaxy luminosities in g' and i' considering absolute solar magnitudes measured by C. Willmer⁵. Finally, we average the individual \mathcal{M}_* estimates and adopt error bars as the standard deviation of the sample of individual measurements. We obtain stellar masses in the range $5.5 \lesssim \log \mathcal{M}_*/M_\odot \lesssim 9.4$. Figure 7 shows the comparison of the derived stellar masses with the apparent and absolute g' -band magnitudes. The corresponding \mathcal{M}_* values, in the following always given in units of M_\odot , are summarized in Table 1.

5. DISCUSSION

5.1. Scaling Relations

Elliptical galaxies are known to fall on a so-called fundamental plane (FP), a tight correlation between effective radius, central velocity dispersion, and the average effective surface brightness within the effective radius (e.g. Faber & Jackson 1976; Faber et al. 1987; Dressler et al. 1987; Djorgovski & Davis 1987; Bender et al. 1992; Burstein et al. 1997; Galazzi et al. 2006). A similar relation was found by Tollerud et al. (2011), showing that dispersion-supported galaxies form a one-dimensional *fundamental curve* in the mass-radius-luminosity space from ultra-faint dwarf spheroidals to giant cluster spheroids. Since the FP shows very little residual scatter it implies very similar mass-to-light ratios and suggests a uniform formation process for bright elliptical galaxies. Projecting the FP onto the luminosity vs. surface-brightness plane, Kormendy (1985) had noted that there seems to be a dichotomy between the scaling relations of bright elliptical galaxies and dwarf galaxies. This dichotomy can be interpreted as the result of different formation mechanisms for giant ellipticals and dwarf spheroidals, but is still hotly debated in the literature (e.g. Binggeli 1994; Graham & Guzmán 2003; Ferrarese et al. 2006; Kormendy et al. 2009; Kormendy & Bender 2012). In order to investigate these possible differences in the formation process of dwarf galaxies in comparison to bright elliptical and spiral galaxies, we plot in Figure 8 the effective radius (r_{eff} , in units of parsec) as a function of stellar mass \mathcal{M}_*/M_\odot and in Figure 9 the effective mass surface density ($\Sigma_{\text{eff}, \mathcal{M}_*} = \mathcal{M}_*/2\pi r_{\text{eff}}^2$, in units of M_\odot/pc^2) as a function of stellar mass \mathcal{M}_*/M_\odot for our NGFS galaxy sample. We put the measurements in the larger context of several other families of stellar systems, covering a wide range in galaxy morphology and stellar mass from low-mass LG dSph galaxies with $\log \mathcal{M}_* \approx 3$ to giant elliptical galaxies at $\log \mathcal{M}_* \approx 12$.

For the subsequent discussion, we divide the $r_{\text{eff}}-\mathcal{M}_*$ and $\Sigma_{\text{eff}, \mathcal{M}_*}-\mathcal{M}_*$ diagrams in two hemispheres with *i*) extended stellar systems ($\log r_{\text{eff}}[\text{pc}] \gtrsim 2.0$), such as dwarf spheroidal galaxies, dwarf elliptical, and giant elliptical (gE) galaxies, and *ii*) compact stellar systems ($\log r_{\text{eff}}[\text{pc}] \lesssim 2.0$) with two subsets, one of which represents globular clusters with two-body relaxation times shorter than a Hubble time (i.e. ob-

⁵ <http://mips.as.arizona.edu/~{ }cnaw/sun.html>

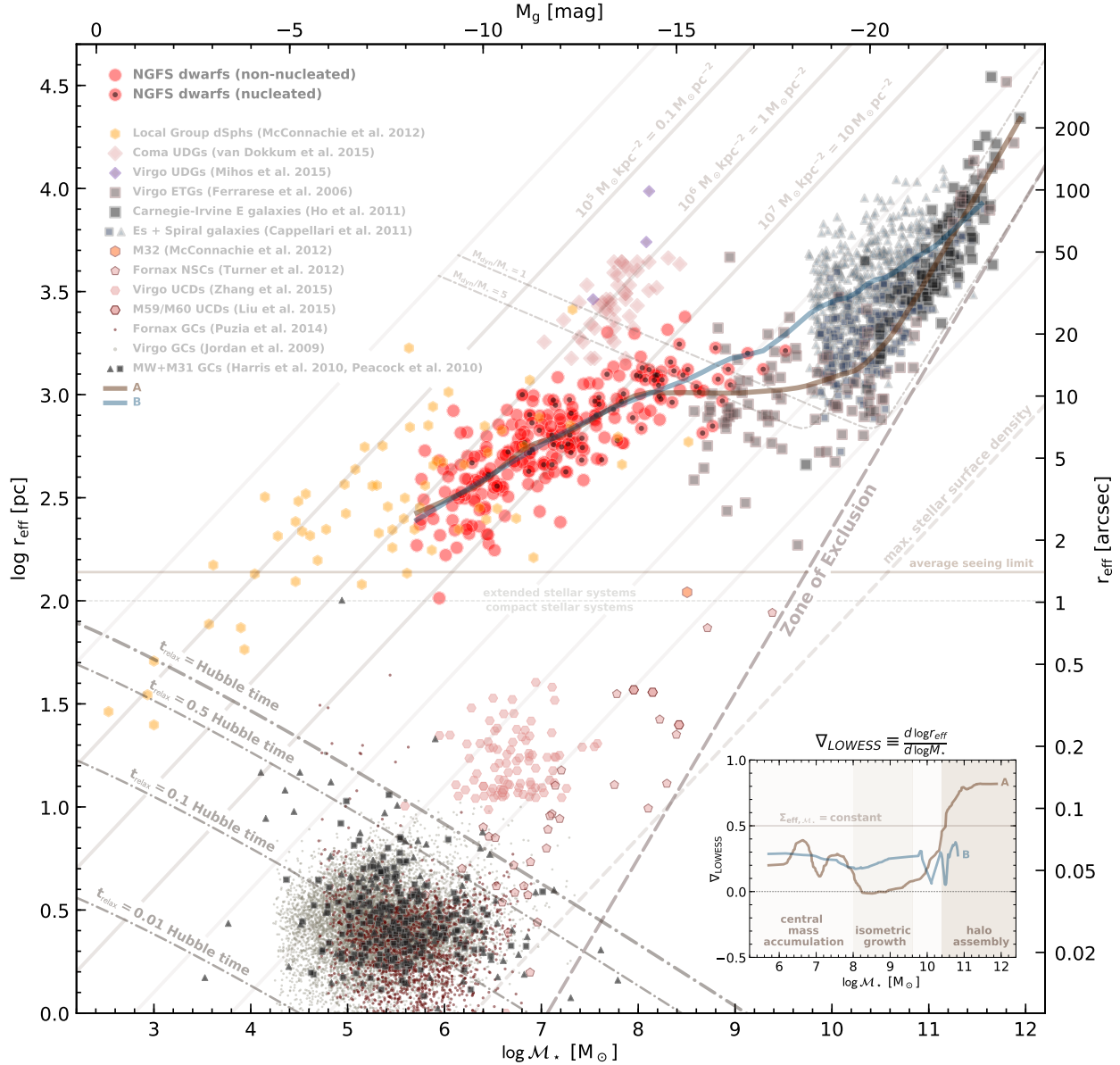


FIG. 8.— Effective radius (r_{eff} in units of parsec) vs. stellar mass (M_* in units of M_\odot) parameter space for NGFS galaxies (red symbols) and various other stellar systems (see legend) with lines of iso- $\Sigma_{\text{eff}, M_*} \equiv M_*/(2\pi r_{\text{eff}}^2)$ indicated. The top ordinate shows the corresponding absolute g' -band luminosity scaled by the average relation from Figure 7. The parameter space is split into extended and compact stellar systems at $r_e = 100$ pc highlighted by the horizontal dotted line. We also show the average seeing limit of our observations measuring ~ 1.4 arcsec. Curves of equal relaxation timescales for $r_e - M_*$ parameter combinations are indicated for various fractions of the Hubble time (thick dash-dotted curves). The Zone of Exclusion (thick dashed line) illustrates the stellar density limit beyond which virtually no objects are found. The line of maximum stellar surface density ($\Sigma_{\text{max}} \approx 10^{11.5} M_\odot \text{kpc}^{-2}$) observed for dense stellar systems in the nearby universe is also indicated (see Hopkins et al. 2010). Similar relations for the ATLAS3D datasets from Cappellari (2016) are plotted for two dynamical to stellar mass ratios, $M_{\text{dyn}}/M_* = 1$ and 5. The brown curve indicates a LOWESS fit to the NGFS dwarfs and other early-type galaxy data from the literature, which the blue curve is a LOWESS fit to the NGFS dwarfs and massive spiral galaxies only. The inset plot in the bottom right corner shows the gradients of these curves with three stellar mass zones dominated by different galaxy mass accumulation processes (see text for details).

jects below the curve $t_{\text{relax}} = \text{Hubble time}$) and the other subset comprising non-relaxed compact stellar systems, such as nuclear star clusters (NSCs) and ultra-compact dwarfs (UCDs). For a description of this part of the parameter space we refer the reader to Misgeld & Hilker (2011). We will not discuss the compact stellar systems further in this work, noting only that numerous recent studies have described the formation scenario of UCDs via tidal stripping of galaxies with NSCs on relatively short timescales (e.g. Bekki et al. 2003; Goerdt et al. 2008; Thomas et al. 2008; Pfeffer & Baumgardt

2013; Pfeffer et al. 2014; Liu et al. 2015; Zhang et al. 2015; Pfeffer et al. 2016). Instead, we focus in the following on the extended stellar systems and the larger galaxy evolution context of our NGFS galaxy sample.

The NGFS sample dwarfs cover stellar masses in the range $\log M_* \approx 5.5 - 9.5$ (see also Fig. 7). The bulk of the NGFS dwarfs show Σ_{eff, M_*} values in the range $\sim 1 - 10 M_\odot \text{pc}^{-2}$ with the most massive dwarfs reaching $\sim 100 M_\odot \text{pc}^{-2}$ (see Figs. 8 and 9). Dwarf galaxies with relatively low stellar masses ($\log M_* \approx 5.5 - 8.0$) follow a scaling relation with

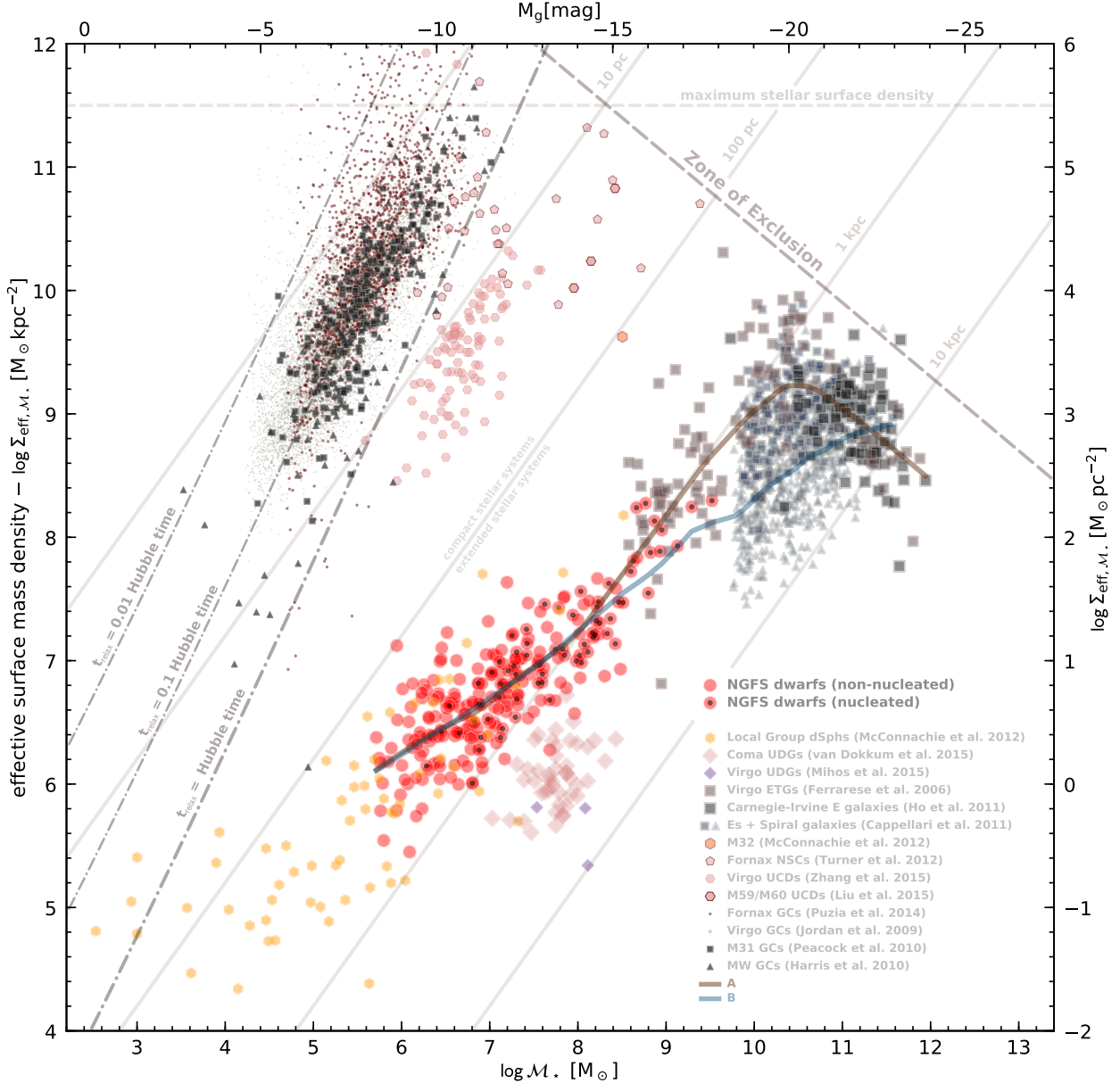


FIG. 9.— Effective surface mass density ($\Sigma_{\text{eff}, \mathcal{M}_*}$) vs. stellar mass (\mathcal{M}_*) parameter space for NGFS galaxies (red symbols) and various other stellar systems (see legend). Solid diagonal lines mark constant effective radius, i.e. iso- r_{eff} lines. Other curves and lines are corresponding to those in Figure 8. The top ordinate shows the corresponding absolute g' -band luminosity scaled by the average relation from Figure 7, while the right abscissa gives the effective surface mass density in units of M_{\odot}/pc^2 .

r_{eff} which is positively inclined with respect to the lines of equal effective surface mass density, i.e. iso- $\Sigma_{\text{eff}, \mathcal{M}_*}$ lines (see diagonal lines in Fig. 8). Meanwhile, recent studies have revealed an expansive population of low-mass dwarfs in the Local Group, including dSphs and UFDs that extend towards even fainter magnitudes (Zucker et al. 2004, 2006a,b; Willman et al. 2005; Belokurov et al. 2006, 2007; McConnachie et al. 2009; Belokurov et al. 2010; McConnachie 2012; Belokurov et al. 2014; Bechtol et al. 2015; Drlica-Wagner et al. 2015; Koposov et al. 2015; Laevens et al. 2015; Homma et al. 2016). Their size-mass-surface density scaling relations appear to line up seamlessly with our NGFS dwarf sample towards lower stellar masses and lower surface mass densities.

We approximate the scaling relations of our NGFS dwarfs

with a Locally Weighted Scatterplot Smoothing (LOWESS) fit (e.g. Cleveland 1981), which is illustrated as a thick curve in Figures 8 and 9. To connect the LOWESS fit of NGFS dwarf sample with more massive galaxies we construct two samples that span the full stellar mass range $\log \mathcal{M}_* \approx 5.5 - 12.0$: **A**) NGFS dwarfs + Virgo ETGs (Ferrarese et al. 2006) + Carnegie-Irvine E galaxies (Ho et al. 2011) shown as a brown curve; and **B**) NGFS dwarfs + spiral galaxies from the ATLAS3D survey⁶ (Cappellari et al. 2011) illustrated as a blue curve. While sample **A** assumes that dwarf galaxies are evolutionary connected to more massive early-type galaxies

⁶ We point out that we do not include the early-type ATLAS3D galaxies in sample **A** due to their relatively shallow stellar mass limit ($\sim 10^{9.5} M_{\odot}$).

through their morphology, sample **B** joins, somewhat *ad hoc*, the dwarf galaxy regime with more massive spirals under the premise that they form a dynamical family in which the angular momentum increases with stellar mass (for a discussion, see Cappellari 2016).

We disregard the class of UDGs for the rest of this work (but see Amorisco & Loeb 2016; Rong et al. 2017, for a theoretical discussion of this galaxy type), but note that the scaling relations in Figures 8 and 9 show a few NGFS objects consistent with massive dwarf galaxy candidates ($7.5 \lesssim \log \mathcal{M}_*/M_\odot \lesssim 8.5$) beginning to encroach upon the parameter space occupied by UDGs, the existence of which has been recently reported in massive galaxy groups and clusters (e.g. van Dokkum et al. 2015; Koda et al. 2015; Mihos et al. 2015; Muñoz et al. 2015; Martínez-Delgado et al. 2016; Merritt et al. 2016; Trujillo et al. 2017; Román & Trujillo 2017b; Janssens et al. 2017; van der Burg et al. 2017; Shi et al. 2017; Bennet et al. 2017; Venhola et al. 2017). UDGs show physical sizes reminiscent of giant galaxies, but \mathcal{M}_* values that put them in the dwarf galaxy mass regime. The result is a systematically lower $\Sigma_{\text{eff}, \mathcal{M}_*}$ that detaches UDGs from the scaling relations shown by the other dwarfs and intermediate stellar-mass galaxies. Given their existence and characteristics one might speculate that these galaxies are dominated by dark-matter, shielding the baryons from the cluster environment (e.g. Mihos et al. 2015; Mowla et al. 2017).

5.2. Scaling Relation Gradients

For sample **A**, we find a galaxy size-mass scaling relation of the form $r_{\text{eff}} \propto \mathcal{M}_*^{0.3 \pm 0.1}$ in the stellar mass range $5.5 \lesssim \log \mathcal{M}_* \lesssim 7.8$, the gradient of which decreases abruptly to zero at $\log \mathcal{M}_* \approx 8.0$ (i.e. $\nabla_{\text{LOWESS}} = \Delta \log r_{\text{eff}} / \Delta \log \mathcal{M}_* \approx 0$, see inset plot in Fig. 8). The effective radius remains virtually independent of stellar mass for more massive galaxies and remains roughly constant at ~ 1 kpc (albeit with a substantial scatter) up to about $\log \mathcal{M}_* \approx 9.5$, where it begins to gently increase again until it jumps abruptly at $\log \mathcal{M}_* \approx 10.5$ to values that are steeper than the iso- $\Sigma_{\text{eff}, \mathcal{M}_*}$ lines. The gradient at high stellar masses ($\log \mathcal{M}_* \gtrsim 10.8$) reaches $r_{\text{eff}} \propto \mathcal{M}_*^{0.75 \pm 0.05}$. For sample **B**, the gradient of the size-mass relation is relatively constant over the entire mass range ($\log \mathcal{M}_* \approx 5.5-12$) around $r_{\text{eff}} \propto \mathcal{M}_*^{0.25 \pm 0.1}$. Although we are dealing with incomplete and partly non-overlapping parameter ranges for the individual datasets depicted in Figures 8 and 9, we observe a smooth transition between the low-mass dwarf regime over the range of intermediate stellar-mass systems to the massive galaxies for our self-consistently observed and analyzed sample of NGFS galaxies. Here, the scaling relations become particularly diagnostic in the intermediate-mass regime ($8.5 \lesssim \log \mathcal{M}_* \lesssim 10.0$), where the association of at least some of the NGFS galaxies with the sample **B** dynamical family cannot be excluded. Testing the internal dynamics of such galaxies is, therefore, of utmost interest. The literature samples are augmenting the information content of the scaling relations for our NGFS data by extending its parameter space coverage, which leads us to the following discussion and interpretation of our measurements.

5.3. Implications for Galaxy Mass Assembly

Dwarf galaxies in cluster environments are believed to have been and some are presently being affected by their environment, which is one of the mechanisms for the creation of the morphology-density or morphology-distance relation

for dwarfs. Environmental effects include tidal stripping, ram pressure stripping, and harassment. Moreover, internal effects may play a role. For instance, winds have been invoked as one of the factors affecting their chemical enrichment, and feedback, in general, may have led to mass loss. How the size-stellar mass (i.e. $r_{\text{eff}}-\mathcal{M}_*$) scaling relation for extended stellar systems can be interpreted in the context of the hierarchical galaxy formation picture has been extensively discussed in the recent literature (for a recent review see Cappellari 2016, and references therein).

Based on the present NGFS data and the comparison with other stellar systems from the literature, the following discussion aims at highlighting the implications of our findings for galaxy mass assembly over a stellar mass range of $5 \lesssim \log \mathcal{M}_* \lesssim 12$. We want to emphasize that this discussion does not necessarily imply an evolutionary sequence in the sense that more massive stellar systems arise from less massive ones observed today. It is merely an empirical observation based on the derived gradients from Sect. 5.2 on how mass assembly occurs in these galaxies at various stellar masses.

First, we note that mass assembly along the iso- $\Sigma_{\text{eff}, \mathcal{M}_*}$ lines implies virtually density-invariant growth, indicating that to first order, mass assembly occurs homologically along these lines, i.e. as galaxies grow in size and stellar mass they retain their surface brightness distribution and, hence, the effective stellar mass surface density.

From Figure 8 we find that as early-type systems (sample **A**) grow in stellar mass, the assembly of baryonic mass must occur in various phases and under the influence of different mechanisms, which depend on the total stellar mass of the system, for the observed relations to emerge. For dwarf galaxies this mass assembly process occurs biased to regions inside the half-light/mass radius since the systems grow disproportionately more dense within r_{eff} as stellar mass increases, i.e. their $r_{\text{eff}}-\mathcal{M}_*$ relation is flatter with respect to the iso- $\Sigma_{\text{eff}, \mathcal{M}_*}$ lines. This trend prevails until \mathcal{M}_* approaches $\log \mathcal{M}_* \approx 8.0$, where the $r_{\text{eff}}-\mathcal{M}_*$ relation becomes flat with significant scatter. The constancy of r_{eff} in this respective mass range had already been pointed out by Smith & Castelli et al. (2008) and Misgeld et al. (2008) and implies that stellar mass is being added both inside and outside the galaxy half-light/stellar-mass radii so that galaxy stellar mass growth occurs without experiencing changes in galaxy sizes, i.e. isometric. Consequently, this mode of stellar-mass growth is accompanied by packing increasingly more stellar mass within the same galaxy dimensions. This process may be triggered by ram-pressure in dense galaxy cluster environments which may temporarily induce enhanced star formation efficiency (e.g. Geha et al. 2012; Wetzel et al. 2013). The isometric stellar mass growth stops when the galaxies reach an apparent maximum stellar mass density of $\Sigma_{\text{eff}, \mathcal{M}_*} \approx 10^4 M_\odot \text{pc}^{-2}$ at around $\log \mathcal{M}_* \approx 10.5$. Beyond this point towards higher \mathcal{M}_* values, galaxy stellar mass accumulation happens predominantly outside their half-light/mass radii, which is consistent with their $r_{\text{eff}}-\mathcal{M}_*$ relations being steeper than the iso- $\Sigma_{\text{eff}, \mathcal{M}_*}$ lines. Similar findings have been put forward by studies of the redshift evolution of the $r_{\text{eff}}-\mathcal{M}_*$ relation of massive galaxies (e.g. Huertas-Company et al. 2013; van Dokkum et al. 2015).

This observed transition from centrally-dominated towards halo-dominated stellar mass accumulation goes hand in hand with the transition from cusp to core-dominated central surface brightness profiles of galaxies more massive than $\log \mathcal{M}_* \approx 9.0$ revealed by HST-based studies (see e.g. Ferrarese et al. 2006; Côté et al. 2007). The homogeneous mor-

phological analysis of our NGFS galaxy dataset, with a much broader stellar mass coverage down to $\log \mathcal{M}_* \approx 5.5$, shows the consistency of this central morphological transition with global Sérsic model parameters. While single-component Sérsic fits represent the majority of our NGFS dwarfs very well (cf. Fig. 4), the surface-brightness profile fits of the most massive NGFS galaxies ($\log \mathcal{M}_* \gtrsim 9.0$) always show residuals, indicative of substructure in single-component fits, requiring up to two additional significant Sérsic components for the brightest systems. This corroborates the idea that the mass-assembly process of dSph and gE galaxies sees the predominance of different mechanisms in action, with the former being mainly assembled through dissipative processes such as wet mergers and gas infall that build the central stellar mass and lead to surface-brightness profiles well represented by single-component Sérsic models (Ferrarese et al. 2006). The gE galaxies, on the other hand, form predominantly via non-dissipative stellar mass accumulation (i.e. dry galaxy mergers) that preserve the phase-space configuration of the infalling material, which results in more complex surface-brightness profiles that are indicative of halo mass accumulation. This bimodal galaxy growth is partly driven by the increasing importance of nuclear feedback processes with increasing total galaxy mass and has been extensively discussed in the recent literature (e.g. Croton et al. 2006; Dekel & Birnboim 2006; Fabian 2012; Kormendy & Ho 2013). Our study delivers a large dwarf galaxy sample, which can be used to constrain the details of quenching mechanisms in today’s high-resolution numerical simulations (e.g. Genel et al. 2017; Bahé et al. 2017).

Future analyses using the NGFS galaxy sample from the entire survey footprint with an augmented SED filter coverage will allow us to conduct more extended in-depth studies as a function of the cluster-centric radius, and search for local anomalies that correlate with particular families of galaxies in the size-mass-surface density parameter space.

6. SUMMARY AND CONCLUSION

This paper is part of a series utilizing newly taken deep $u'g'i'$ photometry from the Next Generation Fornax Survey (NGFS) obtained with the Dark Energy Camera mounted at the prime focus of the Blanco 4-m telescope at the Cerro Tololo Interamerican Observatory in Chile. In the present work we analyze the faint and bright galaxy population in the core of the Fornax galaxy cluster via photometric and structural parameters, measured using the GALFIT software package. In total, 258 dwarf galaxy candidates have been identified by visual inspection of deep RGB image stacks, with galaxy spheroid components reconstructed by single- and multi-component Sérsic models. The current analysis is based on the central $\lesssim 0.25R_{\text{vir}}$ tile of the NGFS survey footprint and will be complemented with the remaining survey data in future work. In the following we summarize our main results:

- The morphological analysis of the dwarf galaxies shows that their spheroid surface-brightness profiles are well represented by single-component Sérsic models with average Sérsic indices in the well-constrained range of $\langle n \rangle_{u',g',i'} = (0.78-0.83) \pm 0.02$, and average effective radii in the range of $\langle r_e \rangle_{u',g',i'} = (0.67-0.70) \pm 0.02$ kpc.
- We find that 75/258 ($\sim 29\%$) of the dwarf galaxy candidates are nucleated based on visual inspection. Compar-

ing galaxy morphologies with total galaxy magnitudes, we find that the nucleation fraction (\mathcal{F}_{nuc}) is a strong function of galaxy luminosity and \mathcal{M}_* . \mathcal{F}_{nuc} shows a strong tendency towards higher fractions in bins containing the brightest galaxies, and declines to 0% for faint galaxies ($M_g' \gtrsim -9$).

- In multi-filter color-magnitude diagrams, the Fornax dwarf galaxy population follows a typical cluster red sequence with brighter galaxies generally exhibiting redder colors. The red sequence slope matches that observed for the dwarf galaxy population in the core of the Virgo cluster. We observe a significant flattening of the red sequence at the faintest galaxy magnitudes, similar to that observed in Virgo. However, the flattening occurs at bluer colors. Because of the color-luminosity relation and the brighter average magnitudes of nucleated dwarfs, the colors of nucleated spheroids are, on average, redder than those of non-nucleated spheroids.
- Bruzual-Charlot SSP models computed for $u'g'i'$ bands indicate that the investigated Fornax dwarf galaxy population is, on average, older than ~ 1 Gyr if the galaxy metallicities are solar-type. Assuming that our dwarf sample exhibits much lower metallicities based on the galaxy mass-metallicity relation, the average dwarf in our NGFS sample is likely older than ~ 5 Gyr. Dwarf galaxy colors are also consistent with a large metallicity spread if the galaxies are uniformly older than ~ 10 Gyr. Spectroscopic information or near-IR photometry is needed to break this age-metallicity degeneracy.
- The Fornax dwarf galaxy population is consistent with known scaling relations between half-light/stellar-mass radius, stellar mass, and stellar mass density for dwarf galaxies, i.e. they follow increasing relations of surface-brightness and/or stellar mass surface density with increasing luminosity and/or stellar mass. For the brightest dwarf galaxies this correlation flattens and reflects the transition towards bright ellipticals showing a presumably more complex formation scenario.
- We find that over the sampled stellar mass range several distinct mechanisms of galaxy mass assembly can be identified: *i*) dwarf galaxies assemble mass inside the half-mass radius up to $\log \mathcal{M}_* \approx 8.0$, *ii*) isometric mass assembly in the range $8.0 \lesssim \log \mathcal{M}_*/M_\odot \lesssim 10.5$, and *iii*) massive galaxies assemble stellar mass predominantly in their halos at $\log \mathcal{M}_* \approx 10.5$ and above.

This project is supported by FONDECYT Postdoctoral Fellowship Project No. 3130750, FONDECYT Regular Project No. 1161817 and the BASAL Center for Astrophysics and Associated Technologies (PFB-06). P.E. acknowledges support from the Chinese Academy of Sciences (CAS) through CAS-CONICYT Postdoctoral Fellowship CAS150023 administered by the CAS South America Center for Astronomy (CASSACA) in Santiago, Chile. M.A.T. acknowledges the financial support through an excellence grant from the Vicerrectoría de Investigación and the Institute of Astrophysics Graduate School Fund at Pontificia Universidad Católica de Chile and the European

Southern Observatory Graduate Student Fellowship program. G.G. acknowledges support from FONDECYT Regular Project No. 1120195. Y.O.-B. acknowledges financial support through CONICYT-Chile (grant CONICYT-PCHA/Doctorado Nacional/2014-21140651). A.L. and M.P. acknowledge ECOS-Sud/CONICYT project C15U02.

This project used data obtained with the Dark Energy Camera (DECam), which was constructed by the Dark Energy Survey (DES) collaboration. Funding for the DES Projects has been provided by the DOE and NSF (USA), MISE (Spain), STFC (UK), HEFCE (UK), NCSA (UIUC), KICP (U. Chicago), CCAPP (Ohio State), MIFPA (Texas A&M), CNPQ, FAPERJ, FINEP (Brazil), MINECO (Spain), DFG (Germany) and the collaborating institutions in the Dark Energy Survey, which are Argonne Lab, UC Santa Cruz, University of Cambridge, CIEMAT-Madrid, University of Chicago, University College London, DES-Brazil Consortium, University of Edinburgh, ETH Zürich, Fermilab, University of Illinois, ICE (IEEC-CSIC), IFAE Barcelona, Lawrence Berkeley Lab, LMU München and the associated Excellence Cluster Universe, University of Michigan, NOAO, University of Nottingham, Ohio State University, University of Pennsylvania, University of Portsmouth, SLAC National

Lab, Stanford University, University of Sussex, and Texas A&M University.

This research has made use of the NASA Astrophysics Data System Bibliographic Services, the NASA Extragalactic Database, the SIMBAD database, operated at CDS, Strasbourg, France (Wenger et al. 2000). This research has made use of "Aladin Sky Atlas" (Bonnarel et al. 2000) developed at CDS, Strasbourg Observatory, France. Software used in the analysis includes the data analysis algorithm GALFIT (v3.0.5; Peng et al. 2010), the astronomical data reduction package IRAF which is distributed by the National Optical Astronomy Observatories (NOAO) as well as the PYTHON/NUMPY v1.11.2 and PYTHON/SCIPY v0.17.0 (Jones et al. 2001; Van Der Walt et al. 2011, <http://www.scipy.org/>), PYTHON/ASTROPY (v1.2.1; Astropy Collaboration et al. 2013, <http://www.astropy.org/>), PYTHON/MATPLOTLIB (v2.0.0; Hunter 2007, <http://matplotlib.org/>), PYTHON/SCIKIT-LEARN (v0.17.1; Pedregosa et al. 2012, <http://scikit-learn.org/stable/>) packages.

Facilities: CTIO (4m Blanco/DECam).

REFERENCES

- Amorisco, N. C., & Loeb, A. 2016, MNRAS, 459, L51
 Asplund, M., Grevesse, N., & Sauval, A. J. 2005, ASPC, 336, 25
 Astropy Collaboration, Robitaille, T. P., Tollerud, E. J., et al. 2013, A&A, 558, 33
 Bahé, Y. M., Barnes, D. J., Dalla Vecchia, C., et al. 2017, MNRAS, 470, 4186
 Baldry, I. K., Glazebrook, K., Brinkmann, J., et al. 2004, ApJ, 600, 681
 Baldry, I. K., Glazebrook, K., & Driver, S. P. 2008, MNRAS, 388, 945
 Baumgardt, H., Cote, P., Hilker, M. et al. 2009, MNRAS, 396, 2051
 Bechtol, K., Drlica-Wagner, A., Balbinot, E., et al. 2015, ApJ, 807, 50
 Bekki, K., Couch, W. J., Drinkwater, M. J., & Shioya, Y. 2003, MNRAS, 344, 399
 Bell, E. F., McIntosh, D. H., Katz, N. et al. 2003, ApJS, 149, 289
 Bell, E. F., Wolf, C., Meisenheimer, K., et al. 2004, ApJ, 608, 752
 Bell, E. F., van der Wel, A., Papovich, C., et al. 2012, ApJ, 753, 167
 Belokurov, V., Zucker, D. B., Evans, N. W., et al. 2006, ApJ, 642, 137
 Belokurov, V., Zucker, D. B., Evans, N. W., et al. 2007, ApJ, 654, 897
 Belokurov, V., Walker, M. G., Evans, N. W., et al. 2010, ApJ, 712, 103
 Belokurov, V., Irwin, M. J., Kposov, S. E., et al. 2014, MNRAS, 441, 2124
 Bender, R., Burstein, D., & Faber, S. M. 1992, ApJ, 399, 462
 Bennet, P., Sand, D. J., Crnojević, D., et al. 2017, arXiv:1710.01728
 Benson, A. J., Bower, R. G., Frenk, C. S., et al. 2003, ApJ, 599, b38
 Bertin, E., & Arnouts, S. 1996, A&AS, 117, 393
 Bertin, E., Mellier, Y., Radovich, M., et al. 2002, Astronomical Data Analysis Software and Systems XI, 281, 228
 Bertin, E. 2006, Astronomical Data Analysis Software and Systems XV, 351, 112
 Binggeli, B., Sandage, A., & Tammann, G. A. 1985, AJ, 90, 1681
 Binggeli, B., Sandage, A., & Tammann, G. A. 1988, ARA&A, 26, 509
 Binggeli, B., & Cameron, L. M. 1991, A&A, 252, 27
 Binggeli, B. 1994, European Southern Observatory Conference and Workshop Proceedings, 49, 13
 Blakeslee, J. P., Jordán, A., Mei, S., et al. 2009, ApJ, 694, 556
 Bonnarel, F., Fernique, P., Bienaymé, O., et al. 2000, A&AS, 143, 33
 Boselli, A., & Gavazzi, G. 2014, A&A Rev., 22, 74
 Bothun, G. D., Impey, C. D., & Malin, D. F. 1991, ApJ, 376, 404
 Brooks, A. M., Kuhlen, M., Zolotov, A., & Hooper, D. 2013, ApJ, 765, 22
 Bruzual, G., & Charlot, S. 2003, ApJ, 694, 556
 Bullock, J. S., Kravtsov, A. V., & Weinberg, D. H. 2001, ApJ, 548, 33
 Bullock, J. S., & Boylan-Kolchin, M. 2017, ARA&A, 55, 343
 Burstein, D., Bender, R., Faber, S., & Nolthenius, R. 1997, AJ, 114, 1365
 Caon, N., Capaccioli, M., & D'Onofrio, M. 1993, MNRAS, 265, 1013
 Cappellari, M., Emsellem, E., Krajnović, D., et al. 2011, MNRAS, 413, 813
 Cappellari, M. 2016, ARA&A, 54, 597
 Chabrier, G. 2003, PASP, 115, 763
 Chen, C.-W., Côté, P., West, A. A., Peng, E. W., & Ferrarese, L. 2010, ApJS, 191, 1
 Chiboucas, K., Karachentsev, I. D., & Tully, R. B. 2009, AJ, 137, 3009
 Chilingarian, I. V., & Zolotukhin, I. Y. 2012, MNRAS, 419, 1727
 Choi, J., Conroy, C., Moustakas, J., et al. 2014, ApJ, 792, 95
 Churazov, E., Forman, W., Vikhlinin, A. et al. 2008, MNRAS, 388, 1062
 Cleveland, W. S. (1981), LOWESS: A program for smoothing scatterplots by robust locally weighted regression, The American Statistician, 35, 54
 Côté, S., Freeman, K. C., Carignan, C. et al. 1997, AJ, 114, 1313
 Côté, P., Ferrarese, L., Jordán, A., et al. 2007, ApJ, 671, 1456
 Crnojević, D., Sand, D. J., Spekkens, K., et al. 2016, ApJ, 823, 19
 Croton, D. J., Springel, V., White, S. D. M., et al. 2006, MNRAS, 365, 11
 D'Abrusco, R., Cantiello, M., Paolillo, M., et al. 2016, ApJ, 819, L31
 Dekel, A., & Birnboim, Y. 2006, MNRAS, 368, 2
 Djorgovski, S., & Davis, M. 1987, ApJ, 313, 59
 Dressler, A., Lynden-Bell, D., Burstein, D., et al. 1987, ApJ, 313, 42
 Drinkwater, M. J., Gregg, M. D., Holman, B. A., & Brown, M. J. I. 2001, MNRAS, 326, 1076
 Drlica-Wagner, A., Bechtol, K., Rykoff, E. S., et al. 2015, ApJ, 813, 109
 Faber, S. M., & Jackson, R. E. 1976, ApJ, 204, 668
 Faber, S. M., Dressler, A., Davies, R. L., Burstein, D., & Lynden-Bell, D. 1987, Nearly Normal Galaxies. From the Planck Time to the Present, 175
 Faber, S. M., Willmer, C. N. A., Wolf, C., et al. 2007, ApJ, 665, 265
 Fabian, A. C. 2012, ARA&A, 50, 455
 Ferrarese, L., Côté, P., Jordán, A. et al. 2006, ApJS, 164, 334
 Ferrarese, L., Côté, P., Cuillandre, J.-C., et al. 2012, ApJS, 200, 4
 Ferrarese, L., Côté, P., Sánchez-Janssen, R., et al. 2016, ApJ, 824, 10
 Ferguson, H. C., & Sandage, A. 1988, AJ, 96, 1520
 Ferguson, H. C. 1989, AJ, 98, 367
 Ferguson, H. C., & Binggeli, B. 1994, A&A Rev., 6, 67
 Flaughner, B., Diehl, H. T., Honscheid, K., et al. 2015, AJ, 150, 150
 Gallazzi, A., Charlot, S., Brinchmann, J., White, S. D. M., & Tremonti, C. A. 2005, MNRAS, 362, 41
 Gallazzi, A., Charlot, S., Brinchmann, J., & White, S. D. M. 2006, MNRAS, 370, 1106
 Gavazzi, G., Boselli, A., Donati, A., Franzetti, P., & Scodreggio, M. 2003, A&A, 400, 451
 Gavazzi, G., Franzetti, P., & Boselli, A. 2014, arXiv:1401.8123
 Geha, M., Blanton, M. R., Yan, R., & Tinker, J. L. 2012, ApJ, 757, 85
 Genel, S., Nelson, D., Pillepich, A., et al. 2017, arXiv:1707.05327
 Gladders, M. D., & Yee, H. K. C. 2005, ApJS, 157, 1
 Goerdt, T., Moore, B., Kazantzidis, S., et al. 2008, MNRAS, 385, 2136
 Graham, A. W., & Guzmán, R. 2003, AJ, 125, 2936
 Grant, N. I., Kuipers, J. A., & Phillipps, S. 2005, MNRAS, 363, 1019
 Graves, G. J., Faber, S. M., & Schiavon, R. P. 2009, ApJ, 693, 486
 Gebel, E. K., Gallagher, J. S., III, & Harbeck, D. 2003, AJ, 125, 1926

- Guo, Q., White, S., Boylan-Kolchin, M., et al. 2011, *MNRAS*, 413, 101
- Harris, W. E. 2010, arXiv:1012.3224
- Hilker, M., Mieske, S., & Infante, L. 2002, *A&A*, 397, L9
- Ho, L. C., Li, Z.-Y., Barth, A. J., Seigar, M. S., & Peng, C. Y. 2011, *ApJS*, 197, 21
- Homma, D., Chiba, M., Okamoto, S., et al. 2016, *ApJ*, 832, 21
- Hopkins, P. F., Murray, N., Quataert, E., & Thompson, T. A. 2010, *MNRAS*, 401, L19
- Huertas-Company, M., Mei, S., Shankar, F., et al. 2013, *MNRAS*, 428, 1715
- Hunter, J. D. 2007, *CISE*, 9, 90
- Impey, C., Bothun, G., & Malin, D. 1988, *ApJ*, 330, 634
- Iodice, E., Capaccioli, M., Grado, A., et al. 2016, *ApJ*, 820, 42
- Janowiecki, S., Catinella, B., Cortese, L., et al. 2017, *MNRAS*, *in press*
- Janssens, S., Abraham, R., Brodie, J. et al. 2017, arXiv:1701.00011
- Jenkins, A., Frenk, C. S., White, S. D. M., et al. 2001, *MNRAS*, 321, 372
- Jones E., Oliphant E., Peterson P., et al. 2001-, SciPy: Open Source Scientific Tools for Python, <http://www.scipy.org/>
- Jordi, K., Grebel, E. K., & Ammon, K. 2006, *A&A*, 460, 339
- Kamada, K., & Long, A. J. 2016, *Phys. Rev. D*, 94, 063501
- Karachentseva, V. E., & Karachentsev, I. D. 1998, *A&AS*, 127, 409
- Karachentseva, V. E., Karachentsev, I. D., & Richter, G. M. 1999, *A&AS*, 135, 221
- Karachentsev, I. D., Karachentseva, V. E., Dolphin, A. E. et al. 2000, *ã*, 363, 117
- Karachentsev, I. D., Tully, R. B., Dolphin, A., et al. 2007, *AJ*, 133, 504
- Kim, H.-S., Yoon, S.-J., Sohn, S. T., et al. 2013, *ApJ*, 763, 40
- King, I. 1962, *AJ*, 67, 471
- Kirby, E. N., Cohen, J. G., Guhathakurta, P. et al. 2013, *ApJ*, 779, 102
- Kleyna, J. T., Wilkinson, M. I., Evans, N. W. et al. 2005, *ApJ*, 630, 141
- Klypin, A., Kravtsov, A. V., Valenzuela, O., et al. 1999, *ApJ*, 522, 82
- Knuth, K. H. 2006, arXiv:physics-0605197
- Koda, J., Yagi, M., Yamanoi, H., & Komiyama, Y. 2015, *ApJ*, 807, 2
- Kodama, T., & Arimoto, N. 1997, *A&A*, 320, 41
- Koposov, S. E., Belokurov, V., Torrealba, G., & Evans, N. W. 2015, *ApJ*, 805, 130
- Kormendy, J. 1985, *ApJ*, 295, 73
- Kormendy, J., Fisher, D. B., Cornell, M. E. et al. 2009, *ApJS*, 182, 216
- Kormendy, J., & Bender, R. 2012, *ApJS*, 198, 2
- Kormendy, J., & Ho, L. C. 2013, *ARA&A*, 51, 511
- Kroupa, P. 2001, *MNRAS*, 322, 231
- Laevens, B. P. M., Martin, N. F., Bernard, E. J., et al. 2015, *ApJ*, 813, 44
- Lauer, T. R., Ajhar, E. A., Byun, Y. I. et al. 1995, *AJ*, 110, 2622
- Le Borgne, J. F., Bruzual, G., Pello, R., et al. 2003, *A&A*, 402, 433
- Lisker, T., Grebel, E. K., Binggeli, B., & Glatt, K. 2007, *ApJ*, 660, 1186
- Liu, C., Peng, E. W., Côté, P., Ferrarese, L. et al. 2015, *ApJ*, 812, 34
- Ma, X., Hopkins, P. F., Faucher-Giguère, C.-A., et al. 2016, *MNRAS*, 456, 2140
- Maiolino, R., Nagao, T., Grazian, A., et al. 2008, *A&A*, 488, 463
- Martínez-Delgado, D., Läsker, R., Sharina, M., et al. 2016, *AJ*, 151, 96
- McConnachie, A. W., Irwin, M. J., Ibata, R. A. et al. 2009, *Nature*, 461, 66
- McConnachie, A. W. 2012, *AJ*, 144, 4
- McLaughlin, D. E., & van der Marel, R. P. 2005, *ApJS*, 161, 304
- Mentz, J. J., La Barbera, F., Peletier, R. F., et al. 2016, *MNRAS*, 463, 2819
- Merritt, A., van Dokkum, P., Danieli, S., et al. 2016, *ApJ*, 833, 168
- Mieske, S., Hilker, M., Infante, L., & Mendes de Oliveira, C. 2007, *A&A*, 463, 503
- Mihos, J. C., Durrell, P. R., Ferrarese, L., et al. 2015, *ApJ*, 809, 21
- Misgeld, I., & Hilker, M. 2011, *MNRAS*, 414, 3699
- Misgeld, I., Mieske, S., & Hilker, M. 2008, *A&A*, 486, 697
- Mistani, P. A., Sales, L. V., Pillepich, A., et al. 2016, *MNRAS*, 455, 2323
- Møller, P., Fynbo, J. P. U., Ledoux, C., & Nilsson, K. K. 2013, *MNRAS*, 430, 2680
- Moore, B., Ghigna, S., Governato, F. et al. 1999, *ApJ*, 524, 19
- Mowla, L., van Dokkum, P., Merritt, A., et al. 2017, arXiv:1710.03762
- Müller, O., Jerjen, H., & Binggeli, B. 2015, *A&A*, 583, 79
- Müller, O., Jerjen, H., & Binggeli, B. 2016, arXiv:1605.04130
- Muñoz, R. P., Puzia, T. H., Lançon, A., et al. 2014, *ApJS*, 210, 4
- Muñoz, R. P., Eigenthaler, P., Puzia, T. H., et al. 2015, *ApJ*, 813, 15
- Murakami, H., Komiyama, M., Matsushita, K., et al. 2011, *PASJ*, 63, S963
- Nelan, J. E., Smith, R. J., Hudson, M. J., et al. 2005, *ApJ*, 632, 137
- Ordenes-Briceño, Y., Taylor, M. A., Puzia, T. H., et al. 2016, *MNRAS*, 463, 1284
- Pedregosa, F., Varoquaux, G., Gramfort, A., et al. 2012, *JMLR*, 12, 2825
- Peng, C. Y., Ho, L. C., Impey, C. D., & Rix, H.-W. 2010, *AJ*, 139, 2097
- Pfeffer, J., & Baumgardt, H. 2013, *MNRAS*, 433, 1997
- Pfeffer, J., Griffen, B. F., Baumgardt, H., & Hilker, M. 2014, *MNRAS*, 444, 3670
- Pfeffer, J., Hilker, M., Baumgardt, H., & Griffen, B. F. 2016, *MNRAS*, 458, 2492
- Poggianti, B. M., Bridges, T. J., Mobasher, B., et al. 2001, *ApJ*, 562, 689
- Powalka, M., Lançon, A., Puzia, T. H., et al. 2016, *ApJS*, 227, 12
- Pritchett, C. J., & van den Bergh, S. 1999, *AJ*, 118, 883
- Read, J. I., Iorio, G., Agertz, O., & Fraternali, F. 2017, *MNRAS*, accepted, arXiv:1607.03127
- Roediger, J. C., Ferrarese, L., Cote, et al. 2016, arXiv:1610.09377
- Roediger, J. C., Ferrarese, L., Côté, P., et al. 2017, *ApJ*, 836, 120
- Román, J., & Trujillo, I. 2017, *MNRAS*, 468, 703
- Román, J., & Trujillo, I. 2017, *MNRAS*, 468, 4039
- Rong, Y., Guo, Q., Gao, L., et al. 2017, arXiv:1703.06147
- Salpeter, E. E. 1955, *ApJ*, 121, 161
- Sánchez-Blázquez, P., Peletier, R. F., Jiménez-Vicente, J., et al. 2006, *MNRAS*, 371, 703
- Sánchez-Janssen, R., Ferrarese, L., MacArthur, L. A., et al. 2016, *ApJ*, 820, 69
- Sandage, A., & Binggeli, B. 1984, *AJ*, 89, 919
- Savaglio, S., Glazebrook, K., Le Borgne, D., et al. 2005, *ApJ*, 635, 260
- Sawala, T., Frenk, C. S., Fattahi, A., et al. 2015, *MNRAS*, 448, 2941
- Sawala, T., Frenk, C. S., Fattahi, A., et al. 2016, *MNRAS*, 456, 85
- Schaye, J., Crain, R. A., Bower, R. G. et al. 2015, *MNRAS*, 446, 521
- Schechter, P. 1976, *ApJ*, 203, 297
- Schlafly, E. F., & Finkbeiner, D. P. 2011, *ApJ*, 737, 103
- Schuberth, Y., Richtler, T., Hilker, M. et al. 2010, *A&A*, 513, 52
- Segers, M. C., Crain, R. A., Schaye, J., et al. 2016, *MNRAS*, 456, 1235
- Sérsic, J. L. 1968, *Atlas de Galaxias Australes* (Córdoba, Argentina: Observatorio Astronómico, 1968)
- Silverman, B. W. 1986, *Monographs on Statistics and Applied Probability*, London: Chapman and Hall, 1986
- Shi, D. D., Zheng, X. Z., Zhao, H. B., et al. 2017, *ApJ*, 846, 26
- Simon, J. D., & Geha, M. 2007, *ApJ*, 670, 313
- Skrutskie, M. F., Cutri, R. M., Stiening, R., et al. 2006, *AJ*, 131, 1163
- Smith Castellì, A. V., Bassino, L. P., Richtler, T. et al. 2008, *MNRAS*, 386, 2311
- Strader, J., Caldwell, N., & Seth, A. C. 2011, *AJ*, 142, 8
- Su, Y., Kraft, R. P., Nulsen, P. E. J., et al. 2017, *ApJ*, 835, 19
- Tammann, G. A. 1994, *Dwarf Galaxies in the Past*, *Dwarf Galaxies*, 49, 3
- Taylor, M. B. 2005, *ASPC*, 347, 29
- Taylor, M. A., Puzia, T. H., Gomez, M., & Woodley, K. A. 2015, *ApJ*, 805, 65
- Taylor, M. A., Puzia, T. H., Muñoz, R. P., et al. 2017, *MNRAS*, 469, 3444)
- Terlevich, A. I., Kuntschner, H., Bower, R. G., Caldwell, N., & Sharples, R. M. 1999, *MNRAS*, 310, 445
- Thomas, D., Maraston, C., Bender, R., & Mendes de Oliveira, C. 2005, *ApJ*, 621, 673
- Thomas, P. A., Drinkwater, M. J., & Evstigneeva, E. 2008, *MNRAS*, 389, 102
- Tollerud, E. J., Bullock, J. S., Graves, G. J., & Wolf, J. 2011, *ApJ*, 726, 108
- Tonry, J. L., Blakeslee, J. P., Ajhar, E. A. et al. 2000, *ApJ*, 530, 625
- Trayford, J. W., Theuns, T., Bower, R. G., et al. 2016, *MNRAS*, 460, 3925
- Tremonti, C. A., Heckman, T. M., Kauffmann, G., et al. 2004, *ApJ*, 613, 898
- Trentham, N., & Tully, R. B. 2002, *MNRAS*, 335, 712
- Trujillo, I., Roman, J., Filho, M., & Sánchez Almeida, J. 2017, *ApJ*, 836, 191
- Turner, M. L., Côté, P., Ferrarese, L., et al. 2012, *ApJS*, 203, 5
- Valdes, F., Gruendl, R., & DES Project 2014, *Astronomical Data Analysis Software and Systems XXIII*, 485, 379
- VanderPlas, J., Connolly, A. J., Ivezić, Z., & Gray, A. 2012, *Proceedings of Conference on Intelligent Data Understanding (CIDU)*, pp. 47-54, 2012., 47
- van der Burg, R. F. J., Hoekstra, H., Muzzin, A., et al. 2017, arXiv:1706.02704
- Van Der Walt, S., Colbert, S. C., & Varoquaux, G. 2011, *Comp. in Sci. and Eng.*, 13, 22
- van de Ven, G., van den Bosch, R. C. E., Verolme, E. K. et al. 2006, *A&A*, 445, 513
- van de Voort, F., Bahé, Y. M., Bower, R. G., et al. 2017, *MNRAS*, 466, 3460
- van Dokkum, P. G., Abraham, R., Merritt, A., et al. 2015, *ApJ*, 798, 45
- van Dokkum, P. G., Nelson, E. J., Franx, M., et al. 2015, *ApJ*, 813, 23
- Venhola, A., Peletier, R., Laurikainen, E., et al. 2017, arXiv:1710.04616
- Vogelsberger, M., Genel, S., Springel, V., et al. 2014, *MNRAS*, 444, 1518
- Wenger, M., Ochsenein, F., Egret, D., et al. 2000, *A&AS*, 143, 9
- Westera, P., Lejeune, T., Buser, R., et al. 2002, *A&A*, 381, 524
- Wetzell, A. R., Tinker, J. L., Conroy, C., & van den Bosch, F. C. 2013, *MNRAS*, 432, 336

TABLE 1
PHOTOMETRIC PROPERTIES AND STELLAR MASSES OF THE DWARF GALAXY SAMPLE

ID	Reference ^a	α (J2000)	δ (J2000)	i' (mag)	g' (mag)	u' (mag)	$(g' - i')_0$ (mag)	$(u' - g')_0$ (mag)	$(u' - i')_0$ (mag)	M_g^b (mag)	$\log \mathcal{M}_*$ (M_\odot)
NGFS033309-352349	FCC114	03 ^h 33 ^m 08 ^s .63	-35°23'49''01	18.67	19.57	20.28	0.90	0.72	1.62	-11.94	7.11
NGFS033311-353956	...	03 ^h 33 ^m 10 ^s .93	-35°39'56''16	20.05	21.62	...	1.57	-9.89	7.05
NGFS033348-355010	FCC125	03 ^h 33 ^m 48 ^s .42	-35°50'09''66	17.64	18.50	19.64	0.86	1.15	2.01	-13.01	7.62
NGFS033350-355706	...	03 ^h 33 ^m 49 ^s .87	-35°57'06''17	20.91	21.57	...	0.66	-9.94	6.24
NGFS033400-354533	...	03 ^h 33 ^m 59 ^s .75	-35°45'33''26	18.30	19.52	20.05	1.22	0.54	1.76	-11.99	7.27
NGFS033406-351638	FCC127	03 ^h 34 ^m 05 ^s .97	-35°16'38''25	18.61	19.39	20.30	0.78	0.92	1.70	-12.12	7.17
NGFS033407-352838	...	03 ^h 34 ^m 06 ^s .97	-35°28'37''99	20.63	22.47	...	1.84	-9.04	6.96
NGFS033409-353100	FCC130	03 ^h 34 ^m 09 ^s .18	-35°30'59''50	17.38	18.10	...	0.72	-13.41	7.68
NGFS033412-351343	FCC131	03 ^h 34 ^m 12 ^s .13	-35°13'43''28	19.15	19.92	20.50	0.77	0.59	1.36	-11.59	6.88
NGFS033414-354910	...	03 ^h 34 ^m 14 ^s .29	-35°49'10''05	19.79	20.47	...	0.68	-11.04	6.70
NGFS033423-355042	...	03 ^h 34 ^m 23 ^s .34	-35°50'41''89	19.18	20.51	...	1.33	-11.00	7.28
NGFS033427-350621	...	03 ^h 34 ^m 27 ^s .18	-35°06'20''76	20.55	21.55	...	1.00	-9.96	6.56
NGFS033433-350236	...	03 ^h 34 ^m 32 ^s .55	-35°02'35''50	20.38	20.62	...	0.24	-10.89	6.23
NGFS033436-360315	...	03 ^h 34 ^m 36 ^s .38	-36°03'15''27	20.56	21.61	...	1.05	-9.90	6.58
NGFS033443-353115	...	03 ^h 34 ^m 43 ^s .39	-35°31'15''07	20.45	21.04	...	0.59	-10.47	6.39
NGFS033446-345334	...	03 ^h 34 ^m 46 ^s .06	-34°53'33''56	20.52	21.29	...	0.77	-10.22	6.45
NGFS033456-351127	FCC140	03 ^h 34 ^m 56 ^s .41	-35°11'27''42	17.61	18.25	19.37	0.64	1.12	1.76	-13.26	7.59
NGFS033458-351324	WFLSB6-2	03 ^h 34 ^m 57 ^s .56	-35°13'24''42	18.72	19.72	20.45	1.00	0.74	1.74	-11.79	7.11
NGFS033458-350235	FCC142	03 ^h 34 ^m 58 ^s .19	-35°02'34''80	17.34	18.37	19.45	1.03	1.08	2.11	-13.14	7.74
NGFS033500-351920	FCC144	03 ^h 35 ^m 00 ^s .20	-35°19'20''26	18.24	19.11	19.83	0.87	0.73	1.60	-12.40	7.28

NOTE. — Table 1 is published in its entirety in the electronic edition of the *Astrophysical Journal*. A portion is shown here for guidance regarding its form and content.

^a Reference to galaxies listed in the FCC catalogue (Ferguson 1989) and in Mieske et al. (2007).

^b Assuming a distance modulus of $(m - M)_0 = 31.51$ mag (Blakeslee et al. 2009).

Willman, B., Dalcanton, J. J., Martinez-Delgado, D., et al. 2005, *ApJ*, 626, 85

Wittmann, C., Lisker, T., Pasquali, A., et al. 2016, *MNRAS*, 459, 4450

Worthey, G. 1994, *ApJS*, 95, 107

Zhang, H.-X., Hunter, D. A., Elmegreen, B. G., Gao, Y., & Schruba, A. 2012, *AJ*, 143, 47

Zhang, H.-X., Peng, E. W., Côté, P. et al. 2015, *ApJ*, 802, 30

Zhang, H.-X., Puzia, T. H., & Weisz, D. R. 2017, arXiv:1710.04214

Zucker, D. B., Kniazev, A. Y., Bell, E. F. et al. 2004, *ApJ*, 612, 121

Zucker, D. B., Belokurov, V., Evans, N. W. et al. 2006, *ApJ*, 643, 103

Zucker, D. B., Belokurov, V., Evans, N. W. et al. 2006, *ApJ*, 650, L41

Zucker, D. B., Kniazev, A. Y., Martinez-Delgado, D. et al. 2007, *ApJ*, 659, 21

Zuhone, J. A., & Roediger, E. 2016, *Journal of Plasma Physics*, 82, 535820301

APPENDIX

DWARF GALAXY SAMPLE PHOTOMETRIC DATA

TABLE 2
 STRUCTURAL PROPERTIES OF THE DWARF SAMPLE

ID	Reference	Type ^a	<i>i'</i>				<i>g'</i>				<i>u'</i>			
			r_e^b	n^c	ϵ^d	PA ^e	r_e^b	n^c	ϵ^d	PA ^e	r_e^b	n^c	ϵ^d	PA ^e
NGFS033309-352349	FCC114	○	0.699	0.81	0.43	98	0.642	0.72	0.47	97	0.584	0.64	0.46	99
NGFS033311-353956	...	○	0.883	0.63	0.24	125	0.757	0.23	0.50	106
NGFS033348-355010	FCC125	○	0.896	0.71	0.15	141	0.866	0.65	0.14	139	0.766	0.50	0.13	150
NGFS033350-355706	...	○	0.435	0.45	0.39	114	0.503	0.50	0.43	136
NGFS033400-354533	...	○	0.563	0.87	0.24	21	0.421	0.63	0.17	30	0.622	1.13	0.30	29
NGFS033406-351638	FCC127	○	0.619	0.82	0.23	72	0.602	0.82	0.22	74	0.526	0.76	0.24	73
NGFS033407-352838	...	○	0.623	0.82	0.13	173	0.359	0.30	0.16	118
NGFS033409-353100	FCC130	○	1.819	0.80	0.17	135	2.008	0.91	0.18	130
NGFS033412-351343	FCC131	⊙	0.526	0.75	0.44	127	0.521	0.91	0.47	128	0.475	0.72	0.34	109
NGFS033414-354910	...	○	0.634	0.39	0.17	2	0.715	0.57	0.25	179
NGFS033423-355042	...	○	0.848	0.73	0.21	98	0.673	0.41	0.15	69
NGFS033427-350621	...	○	0.466	0.95	0.42	26	0.356	0.68	0.32	33
NGFS033433-350236	...	○	0.499	0.78	0.36	100	0.657	0.69	0.39	99
NGFS033436-360315	...	○	0.573	0.62	0.51	168	0.467	0.50	0.36	179
NGFS033443-353115	...	○	0.377	0.74	0.09	99	0.400	0.73	0.11	89
NGFS033446-345334	...	⊙	0.440	0.65	0.29	140	0.410	0.67	0.22	98
NGFS033456-351127	FCC140	⊙	0.898	0.81	0.46	95	0.968	0.89	0.47	94	0.795	0.63	0.47	94
NGFS033458-351324	WFLSB6-2	○	0.559	1.00	0.29	41	0.508	0.80	0.31	50	0.486	0.65	0.30	54
NGFS033458-350235	FCC142	⊙	1.011	1.34	0.06	134	0.847	1.02	0.06	149	0.708	0.92	0.11	16
NGFS033500-351920	FCC144	○	0.597	0.81	0.23	56	0.592	0.77	0.25	56	0.523	0.82	0.23	55

NOTE. — Table 2 is published in its entirety in the electronic edition of the *Astrophysical Journal*. A portion is shown here for guidance regarding its form and content.

^a Morphological galaxy type classification: ⊙=nucleated, ○=non-nucleated dwarf galaxy.

^b Effective radii given in kpc.

^c Sérsic index (Sérsic 1968; Caon et al. 1993).

^d Ellipticity $\epsilon = 1 - b/a$.

^e Position angle in $^\circ$ from North towards East.